Petrophysics of fine-grained mass-transport deposits: a critical review

Qiliang Sun[a,b,c,d,*], Tiago Alves[e]

[a]*College of Marine Science and Technology, China University of Geosciences (CUG), Wuhan, Hubei 430074, PR China;*

[b]*Laboratory for Marine Mineral Resources, Qingdao National Laboratory for Marine Science and Technology, Qingdao 266061, China;*

[c]*Key Laboratory of Tectonics and Petroleum Resources, China University of Geosciences, Ministry of Education, Wuhan 430074, China;*

[d]*Department of Earth Sciences, University of Oxford, Oxford OX1 3AN, United Kingdom;*

[e]*3D Seismic Lab, School of Earth and Ocean Sciences, Cardiff University, Main Building, Park Place, Cardiff CF10 3AT, United Kingdom;*

Highlights

1. Fine-grained MTDs comprise a 'main body' and a 'basal shear zone';

2. The main bodies of MTD have contrasting petrophysical properties to their basal shear zones;

3. The main bodies of MTD tend to form a seal interval, whilst the basal shear zone are carriers of fluid;

4. Basal shear zones of MTDs can comprise weak layers promoting further slope instability.

Abstract:

*Corresponding author: Dr. Qiliang Sun
Telephone/fax: +86 27 67886167
E-mail address: sunqiliang@cug.edu.cn.

Submarine slope failures and their products occur at variable scales on continental margins and island flanks. Here, we review the petrophysics of fine-grained mass-transport deposits (MTDs) from three representative regions: the Ulleung Basin from offshore Korea, the Ursa Region in the Gulf of Mexico, and the Amazon Fan in the Equatorial Brazil. This study shows that fine-grained MTDs comprise a 'main body' and a 'basal shear zone'. Compared to undeformed 'background' hemipelagic sediments, the main bodies of all studied MTDs are characterised by their: (1) higher resistivity, density, velocity and shear strength, and (2) lower water content, porosity and permeability. These properties indicate that MTDs are more consolidated than 'background' undeformed strata due marked dewatering and shear compaction during their emplacement, thus enhancing the sealing competence of such strata. However, the basal shear zones show contrasting petrophysical trends, recording an increase in porosity when compared to the main MTD bodies. This suggests that the fractured basal shear zones of MTDs serve as main fluid paths, and fluids can accumulate within or laterally migrate along them. This study ends by postulating that dipping strata on continental slopes can likely fail under its own gravity, with fractured, gas-charged basal shear zones at the base of MTDs comprising weak layers for further slope instability.

Keywords:

Mass-transport deposits; fluid migration; petrophysics; seal competence; IODP/ODP; Gulf of Mexico; Ulleung Basin; Amazon Fan

1. Introduction

MTDs are a common component of continental margins and island flanks around the world. They have been extensively studied over the past few decades, because of their significant roles in: (1) reshaping the morphology of continental margins, (2) controlling the sedimentary architectures of continental slope basins (e.g. Posamentier and Kolla, 2003; Gee et al., 2006; Moscardelli et al., 2006; Moscardelli and Wood, 2008; Gong et al., 2014), (3) transporting large volumes of sediment into deep-water areas (e.g. Weimer, 1989; Frey-Martínez et al., 2005; Gee et al., 2006; Masson et al., 2006; Lee and Stow, 2007; Moscardelli and Wood, 2008; Li et al., 2015), and (4) generating catastrophic near-seafloor geohazards (e.g. Locat and Lee, 2002; Krastel et al., 2006; Masson et al., 2006; Alves, 2015).

Most studies of MTDs have thus far been based on geophysical data (e.g. multi-channel seismic, multibeam bathymetry and sidescan sonar data) and, as a result, the external morphologies and internal characters of such deposits are well known at a decametric (10 m) scale (e.g. McAdoo et al., 2000; Posamentier, 2004; Sawyer et al., 2007; Moscardelli and Wood, 2008; Bull et al., 2009). Mass-transport deposits have also been sampled by the DSDP/ODP/IODP drilling consortia and by exploration wells. Their general petrophysical characters (e.g. a tendency for a relative increase in density and a reduction in porosity) have confirmed that MTDs chiefly comprise seal intervals in sedimentary basins (e.g. Piper et al., 1997; Shipp et al., 2004; Sawyer et al., 2007; Dugan, 2012; Reece et al., 2012; Riedel et al., 2012; Hornbach et al., 2015; Gardona et al., 2016; Bahk et al., 2017). Nevertheless, the scientific community recognises that the

petrophysical characters of MTDs are still insufficiently addressed due to a relative lack of core samples and well-log data (e.g. Shipp et al., 2004; Dugan, 2012; Alves et al., 2014). Previous works have also been focused on discrete case studies, and broad syntheses using data from distinct continental margins has seldom been completed. In order to improve the current knowledge on the petrophysical characters of MTDs, and to better assess their seal competence, one needs to: (1) quantitatively analyze the petrophysical character of distinct MTDs, (2) integrate distinct datasets and lithological information from different continental margins with MTDs, and (3) explore the variability in the petrophysical characters of MTDs and their underlying geological causes.

To understand the petrophysical character and seal competence of MTDs is particularly important on continental margins where petroliferous basins are located and fluid (e.g. hydrocarbon) migration is active. MTDs triggered by fluid migration occurs at present (e.g. Sultan et al., 2004; Flemings et al., 2008), but the opposite scenario in which fluid migration is controlled by MTDs is still poorly understood (Sun et al., 2017). Though they are primarily interpreted as competent seal intervals, thus preventing vertical fluid migration (e.g. Shipp et al., 2004; Alves et al., 2014), strata disaggregation in MTDs, reflected as variations in their structural and petrophysical properties, may also result in the migration and escape of fluid to the surface (e.g. Paull et al., 2003; Bünz et al., 2005; Flemings et al., 2005; Masson et al., 2006). There is also limited knowledge about how homogeneous and predictable is seal competence in the largest MTDs at different depths (from top to base) and in the three dimensions (3D).

This study uses well-log data from IODP/ODP Expeditions 308 and 155, and an exploration well from the Ulleung Basin in South Korea (Riedel et al., 2012) (Fig. 1). Several MTDs were drilled by these wells and their general petrophysical characters are reported in previous studies (e.g. Piper et al., 1997; Sawyer et al., 2007, 2009; Dugan, 2012; Reece et al., 2012; Riedel et al., 2012; Bahk et al., 2017). In this study, we aim to:

(1) quantitatively analyse and summarise the petrophysical characters of MTDs in three representative regions, based on our detailed observations and previous work (e.g. Piper et al., 1997; Sawyer et al., 2007; Dugan, 2012; Riedel et al., 2012);
(2) understand horizontal and vertical seal heterogeneity in MTDs;
(3) propose a formation model for slope failures, discussing the types of geohazards related to them.

Compared to previous work, our study is quantitative and described in more detail, focusing on understanding the differences of petrophysical characters between MTDs and undeformed strata, and also between different parts of an MTD ("main body" and "basal shear zone"). This work also provides new data concerning the petrophysical characters of MTDs (see following section).

2. Data and methods

Logging-while-drilling (LWD) data (resistivity, gamma ray, bulk density, porosity,

compression velocity, shear strength and water content) from IODP Sites U1322, U1323 and U1324 of Expedition 308 (Ursa Region in the Gulf of Mexico), and ODP Sites 933, 936 and 941 of Expedition 155 (Amazon Fan), plus wireline data collected from exploration well UBGH 1-4 (Ulleung Basin, offshore Korea), are used to address the petrophysical properties of representative MTDs in these regions. Most of the IODP and ODP data are available on http://brg.ldeo.columbia.edu/logdb/files.php, http://www-odp.tamu.edu/publications/pubs_pr.htm and http://publications.iodp.org/.

Data from exploration well UBGH 1-4 is based on Riedel et al. (2012). These data are publicly available and were used in previous studies to address the presence of gas hydrates and fluid flow (e.g. Long et al., 2011; Riedel et al., 2012), local sedimentation rates (e.g. Pirmez et al., 1997; Patricia et al., 1997; Yu et al., 2008), and the development of slope instability features offshore South Korea (e.g. Piper et al., 1997; Sawyer et al., 2009; Urgeles et al., 2010; Dugan, 2012; Riedel et al., 2012). In this study, we mainly focus our attention on the petrophysical characters of strata within and involving discrete MTDs.

The interpreted wireline data was loaded into *Resform* software. Sediment porosity (ø) values from IODP Expedition 308 were calculated from the bulk density (ρ_b) data using the method of Dugan (2012). Porosity is defined as $ø = (\rho_b - \rho_g)/(\rho_w - \rho_g)$, where ρ_g and ρ_w are solid-grain density and pore-fluid density, respectively. Based on the observed porewater chemistry and measured grain density, the standard seawater density is 1.024 g/cm^3 and the constant grain density is 2.7 g/cm^3 in the Gulf of Mexico (Flemings et al., 2005; Dugan, 2012).

3. Results

3.1. Petrophysical character of MTDs in the Gulf of Mexico

Six sites were drilled in the Brazos-Trinity Basin and Ursa Region, Gulf of Mexico, during IODP Expedition 308, held in 2005 (Fig. 1). MTDs were crossed at four sites (IODP Sites U1320, U1322, U1323 and U1324; Expedition 308 Scientists, 2005), and their general petrophysical characters have been described by previous studies (e.g. Sawyer et al., 2009; Dugan, 2012; Reece et al., 2012). Here, we focus on three sites (IODP Sites U1322, U1323 and U1324) in which fine-grained MTDs accumulated.

3.1.1. IODP Site U1322

IODP Site U1322 drilled clay and mud to a depth of ~234.5 meters below the sea floor (mbsf). Four MTDs, MTD1 to 4, are identified on wireline data (Fig. 2). At IODP Site U1322, resistivity increases from ~0.52 to ~0.95 ohm·m above MTD 1 (Fig. 2). It jumps slightly to ~0.98 ohm·m at the top of MTD 1, quickly reaching a maximum of ~ 1.22 ohm·m at ~53.6 mbsf. It quickly decreases to ~1.05 ohm·m at the base of this same MTD (Fig. 2). Peaks in resistivity are also observed at the tops of MTD 2, MTD 3 and MTD 4. For example, resistivity increases from ~1.20 to ~1.22 ohm·m at the top of MTD 2. Conversely, lower resistivity values are observed at the bases of MTD 2, MTD3 and MTD 4 (Fig. 2).

Gamma-ray values are highly variable, but no obvious differences are observed

between MTDs and undeformed strata (Fig. 2).

The bulk density of MTD 1 increases at its top until it reaches a maximum of ~ 1.76 g/cm^3. It then decreases to ~1.70 g/cm^3 at its base (Fig. 2). Similarly to MTD 1, bulk density sharply increases from ~1.80 g/cm^3 to ~1.85 g/cm^3 at the top of MTD 2. It gradually reaches ~1.98 g/cm^3 at ~118.6 mbsf within MTD 2, and then decreases to ~1.85 g/cm^3 at its base (Fig. 2). The bulk density of MTD 4 has a similar character to MTDs 1 and 2. However, the bulk density in MTD 3 decreases from its top (~1.96 g/cm^3) to its base (~1.89 g/cm^3). In general, average bulk density is higher in MTDs than that in undeformed strata (Fig. 2). For instance, MTD 2 is ~8.4% and ~3.2% denser than undeformed strata above and below.

Porosity gradually decreases below the sea floor (Fig. 2). In addition, both the tops and bases of MTDs 1, 2 and 4 are marked by sharp porosity changes (Fig. 2). The porosity of MTD 1 decreases from ~65% at its top to a minimum of ~55.5% at 57.6 mbsf. It then increases to ~59.6% at its base (Fig. 2). MTD 2 has similar trend to MTD 1. Its porosity decreases from ~53.1% at its top to ~43.0% at ~118.7 mbsf, increasing to ~50.5% at its base (Fig. 2). The average porosity of MTD 2 is ~11.4% and ~3.3% lower than the porosities of undeformed strata confining it. The porosity of MTD 3 increases from ~43.3% at its top to ~46.9% at its base, showing an average porosity of ~44.6%. The porosity of MTD 4 is similar to that of MTD 1. It decreases to a minimum of ~44.4% at ~190.0 mbsf, to increase once again at its base (Fig. 2).

3.1.2. IODP Site U1323

IODP Site U1323 drilled through 241 m of hemipelagic mud (0-195 mbsf) and silty sand (195-241 mbsf) (Fig. 3). Two MTDs are identified on seismic and wireline data at this site. The shallower, mud-dominated MTD 5 is ~9 m thick (41-50 mbsf). The deeper MTD 6 is also mud dominated, but shows thin silt intervals (3-6 m). MTD 6 is ~98 m thick, occurring between 97 and 195 mbsf (Fig. 3).

At IODP Site U1323, resistivity increases from ~0.5 to ~1.4 Ohm·m in the first 195 m, within mud-dominated sediments (Fig. 3). Two sharp increases in resistivity, corresponding to the tops of MTDs, are observed. For example, resistivity increases from ~1.06 to ~1.30 Ohm·m at the top of MTD 6; the average resistivity of MTD 5 and MTD 6 is ~18% and ~23.6% higher than undeformed strata above, and ~8% and ~24.8% higher when compared with undeformed strata below (Fig. 3; Table 1). Compared to muddy undeformed sediment, the silty intervals drilled within and below MTD 6 have low resistivity.

There are minor differences in the gamma-ray curves when comparing MTDs with undeformed strata (Fig. 3). In general, gamma-ray values in the mud are much higher than in silt- or sand-dominated sediments (Fig. 3; Table 1).

The bulk density of MTD 5 increases sharply at its top and keeps increasing to a maximum of ~1.68 g/cm^3 at its base. The average bulk density of MTD 5 is slightly higher than undeformed strata (Table 1). There is a ~0.1 g/cm^3 jump in bulk density at the top of MTD 6. Bulk density then remains constant at ~2.0 g/cm^3 from 120 to 184 mbsf, with only two drops in density that correspond to silt/sand intervals (Fig. 3). At the base of MTD 6 (184 - 195 mbsf), the bulk density decreases markedly and is ~12%

lower than the average bulk density of MTD strata above. The bulk density of the silt/sand interval below MTD 6 gradually increases to ~1.86 g/cm^3, remaining constant until the bottom of IODP Site U1323 (Fig. 3). In general, the average bulk density of MTD 6 is ~7% higher than that of undeformed strata (Table 1).

Porosity has a negative relationship with bulk density at IODP Site U1323; it gradually decreases from ~66% at the top of MTD 5 to ~60% at its base (Fig. 3). The average porosity of MTD 5 is ~4.5% and ~3% lower than the average porosities of undeformed strata above and below, respectively (Table 1). Porosity gradually decreases to ~43% at 120 mbsf. Except for two small increases that correspond to silty intervals, porosity is mostly constant with a minor fluctuation from 120 to 184 mbsf (Fig. 3). However, porosity increases markedly at the base of MTD 6 (184 - 195 mbsf), where is ~28.3% higher than the average porosity of MTD strata above. The porosity of silt/sand intervals below MTD 6 gradually decreases to ~52% and is constant until the bottom of IODP Site U1323 (Fig. 3). In general, the average porosity of MTD 6 is ~14.3% lower than the porosity of undeformed sediments (Table 1).

3.1.3. IODP Site U1324

IODP Site U1324 terminates at 612 mbsf and crosses a 57 m-thick MTD 7 (110-167 mbsf) that is mud-dominated (Fig. 4). MTD 7 is characterised on seismic data by its chaotic internal reflections and marked top and basal surfaces (Fig. 4). Changes in resistivity, gamma ray, density and porosity are less marked at the top of MTD 7 than at its base (Fig. 4). In terms of resistivity, there is a minor increase (~0.06 Ohm·m) at

the top of MTD 7, to then gradually increase with depth to an average of ~1.23 Ohm·m (Fig. 4). At the base of MTD 7, resistivity decreases sharply to ~1.1 Ohm·m (Fig. 4).

Gamma-ray values at IODP Site U1324 decrease from ~78.0 to ~69.0 gapi from undeformed strata towards MTD 7 (Fig. 4). In MTD 7, gamma-ray values increase to ~81.5 gapi from its top to ~133 mbsf, and then decrease to ~62.0 gapi from 133 to 159 mbsf. At the base of MTD 7, the gamma ray increases again and reaches a maximum of ~82.0 gapi at 166 mbsf (Fig. 4).

Bulk density increases to ~2.0 g/cm^3 from the sea floor to 150 mbsf, and remains constant at ~2.0 g/cm^3 from 150 to 162 mbsf (Fig. 4). The bulk density sharply decreases at the base of MTD 7 (162 - 166 mbsf) where a minimum of ~1.78 g/cm^3 is reached.

The porosity of MTD 7 shows a negative relationship with the bulk density curve. It increases sharply to reach to ~55% at the base of MTD 7 (Fig. 4). The porosity of undeformed sediments below MTD 7 is nearly constant, with an average bulk density of ~46.7%.

3.2. Petrophysical character of MTDs in the Ulleung Basin, South Korea

Exploration wells were drilled in the Ulleung Basin in 2007 and 2010 to verify the presence of gas hydrates. MTDs were found in several wells (e.g. UBGH1-4, UBGH1-14, UBGH2-4, UBGH2-5A and UBGH2-8) (Riedel et al., 2012, 2013; Ryu et al., 2012; Bahk et al., 2017). Wireline data for UBGH 1-4 is re-assessed in this work.

UBGH 1-4 crossed a mud-dominated succession comprising three distinct MTDs

(Fig. 5). The shallower MTD 8 is ~9 m thick (~38 - 47 mbsf), whereas the deeper MTD 10 is only ~4 m thick (~146 - 150 mbsf). MTD 9 at the middle of the drilled succession has a thickness of ~56 m from ~66 to 122 mbsf (Fig. 5).

In UBGH 1-4, resistivity increases to ~1.4 ohm·m at the top of MTD 8, dropping to ~0.8 ohm·m at its base (Fig. 5). The resistivity sharply increases from ~0.8 to 1.4 ohm·m at the top of MTD 9 (Fig. 5). It fluctuates between ~1.2 and ~1.4 ohm·m in MTD 9, with a sharp increase between 112 and 115 mbsf (maximum of ~1.8 ohm·m). It decreases to ~1.1 ohm·m at the base of MTD 9 (Fig. 5). The resistivity of MTD 10 has a similar pattern to MTDs 8 and 9, increasing to ~1.5 ohm·m at its top and dropping to ~0.8 ohm·m at its base (Fig. 5).

Gamma-ray curves do not reveal differences between MTDs and undeformed strata (Fig. 5). In MTD 9, gamma-ray values decrease slightly in its upper part, to then increase in its lower half (Fig. 5). There is a minor drop in gamma-ray values at the base of MTD 9 (Fig. 5).

P-wave velocity (Vp) increases to ~1540 m/s from ~1480 m/s at the top of MTD 8 (~36- 41 mbsf), dropping to ~1490 m/s at its base (~44 - 46 mbsf) (Fig. 5). Vp values are nearly constant (~1490 - 1500 m/s) in the strata separating MTD 8 and MTD 9. Vp values increase to ~1580 m/s at the top of MTD 9 and are kept between 1550 m/s and 1700 m/s, values that are ~10.0% higher than those of undeformed strata. Vp decreases markedly at the base of MTD 10 (119 - 122 mbsf) (Fig. 5). Except for a Vp maximum of ~1700 m/s in MTD 10, the strata below MTD 10 show Vp values between ~1520 m/s and ~1580 m/s, with moderate variations (Fig. 5).

Bulk density increases from ~1.4 g/cm^3 to ~1.85 g/cm^3 at the top of MTD 8, dropping to ~1.4 g/cm^3 at its base (Fig. 5). Bulk density also increases at the top of MTD 9, ranging from ~1.6 g/cm^3 to ~2.0 g/cm^3 within this latter MTDs (Fig. 5). At the base of MTD 9 (~119 - 122 mbsf), the bulk density decreases sharply to ~1.75 g/cm^3 (Fig. 5). The bulk density of strata underlying MTD 9 ranges from ~1.5 g/cm^3 to ~1.7 g/cm^3 (Fig. 5).

Neutron porosity gradually decreases from the sea floor to the lower part of MTD 8. However, porosity increases to ~64% at the base of MTD 8 (Fig. 5). Porosity gradually decreases below the top of MTD 9; it ranges between ~48 and ~52% from ~77 to ~99 mbsf. It varies markedly between ~99 and ~112 mbsf to reach a maximum of ~60% at ~112 mbsf (Fig. 5). From ~112 to ~119 mbsf, the porosity gradually decreases to ~42% at ~119 mbsf, quickly increasing to ~54% at the base of MTD 9 (~119 - 122 mbsf). Except for a large drop in porosity within MTD 10 (to a minimum of ~40%), the porosity of strata below MTD 9 ranges between ~52 and 60%, with moderate variations (Fig. 5).

3.3. Petrophysical character of MTDs in the Amazon Fan

MTDs were penetrated at ODP Sites 931, 933, 935, 936, 941 and 944 (ODP Leg 155), where they are intercalated with thick, predominately muddy, channel-levee deposits (Piper et al., 1997). The petrophysical characters of MTDs at ODP Sites 933, 936 and 941, which drilled fine-grained sediments, are analyzed. Compared to the latest IODP and exploration well data, as referred to in the previous sections, ODP Leg 155 was

drilled in 1994, sampling cores at intervals of 1.0 to 6.0 m. Therefore, we could only rely on the trends of well-log data and could not identify detailed variations in petrophysical properties, especially at the tops and bases of MTDs. In other words, the main body of MTDs, and their basal shear zones, are not well resolved in the Amazon Fan sites (Fig. 6).

3.3.1. ODP Site 933

ODP Site 933 has a total length of cored section approaching 254.2 m, in which a mass-transport deposit (MTD 11) with a thickness of ~70 m (~97.6-167.3 mbsf) was drilled (Fig. 6).

The porosity of ODP Site 933 gradually decreases from the sea floor to the bottom of the well. Porosity greatly decreases at the top of MTD11, increasing at its base (Fig. 6a). For example, the porosity of MTD 11 decreases to ~50.8% from ~52% at its top and increases to ~58.1% from ~44.6% at its base. The porosity of MTD 11 ranges from ~41.1 to ~50.8%, with an average of ~45.8%. This is ~15.6% and ~14.2% lower than the average porosity of undeformed strata above (~54.3%) and below (~53.4%) MTD 11 (Fig. 6a).

Resistivity is highly variable and generally increases with depth (Fig. 6b). It increases from ~0.39 ohm·m in undeformed strata to ~0.45 ohm·m at the top of MTD 11 (Fig. 6b). It also decreases from ~0.54 ohm·m at the base of MTD 11 to ~0.36 ohm·m in undeformed strata below MTD 11. In general, MTD 11 has an average resistivity of ~0.47 ohm·m that is ~9.3% and ~17.5% higher than undeformed strata above (with an

average of ~0.43 ohm·m within a ~20 m interval) and below (average of ~0.40 ohm·m within a ~30 m interval).

MTD 11 is denser than undeformed strata above and below (Fig. 6c). The density increases from ~1.87 g/cm^2 to ~1.92 g/cm^2 at the top of MTD 11, and decreases to ~1.79 g/cm^2 from ~2.04 g/cm^2 at the base of MTD 11. In general, MTD 11 has an average density of ~2.00 g/cm^2, ranging from ~1.91 to 2.11 g/cm^2. It is ~6.4% higher than undeformed strata above (~1.88 g/cm^2 within a ~20 m interval) and below (~1.88 g/cm^2 within a ~30 m interval).

3.3.2. ODP Site 936

ODP Site 936 drilled ~300 m of muddy deposits. A ~141 m thick MTD 12 was crossed from ~153 to 294 mbsf (Fig. 6).

Similarly to ODP Site 933, porosity gradually decreases with depth (Fig. 6a). Porosity decreases from ~52.1% in undeformed strata above MTD 12 to ~45.9% at its top. It increases from ~40% of the base of MTD 12 to ~45.3% in undeformed strata below. The average porosity of MTD 12 is ~44%, varying from ~39.1% to 53.3% (Fig. 6a). These values are ~19.1% and ~3.6% lower than the average porosity of undeformed strata above (average of ~54.4% in a ~50 m-thick interval above MTD 12) and below (with an average porosity of ~45.7% in a ~10 m-thick interval below MTD 12).

The resistivity of MTD 12 at ODP Site 936 ranges between ~0.41 ohm·m and ~0.73 ohm·m with an average of ~0.51 ohm·m (Fig. 6b). It is ~24.4% and ~8.5% higher than the average resistivity of undeformed strata above (~0.41 ohm·m within a ~40 m

interval) and below (~0.47 ohm·m within a ~10 m interval). Moreover, the resistivity varies sharply at the boundaries between MTD 12 and undeformed strata (Fig. 6b). For example, it increases from ~0.42 ohm·m to ~0.48 ohm·m at the top of MTD 12, and decreases from ~0.61 ohm·m to ~0.44 ohm·m at the base of MTD 12.

MTD 12 has a higher density compared to undeformed strata (Fig. 6c). The density increases to ~2.03 g/cm^2 from ~1.87 g/cm^2 at the top of MTD 12, and decreases to ~2.00 g/cm^2 from ~2.13 g/cm^2 at its base. In general, the average density of MTD 12 is ~2.04 g/cm^2, ranging between ~1.84 g/cm^2 and 2.15 g/cm^2. It is ~9.1% and ~1.0% larger than the density of undeformed strata above (average of ~1.87 g/cm^2 in a ~40 m-thick interval above MTD 12) and below (with an average of ~2.02 g/cm^2 in a ~10 m-thick interval below MTD 12).

3.3.3. ODP Site 941

ODP Site 941 drilled to a depth of ~177.9 mbsf and crossed a shallow MTD 13 from ~5.3 mbsf to ~129.7 mbsf (Fig. 6a).

The porosity of MTD 13 ranges from ~44.3% to ~64.3% and has an average of ~54.8%. It is ~8.1% higher than the average porosity of undeformed strata below (average of ~50.7% in a ~20 m-thick interval), but ~26.7% lower than the average porosity of undeformed strata above (~74.8%, ~5.3 m). Porosity increases from ~49.4% at the base of MTD 13 to ~51.3% in undeformed strata below. It also increases from 64.2% at the top of MTD 13 to ~74.8% in undeformed strata above (Fig. 6a).

Resistivity varies sharply across the upper and lower boundaries of MTD 13 (Fig.

6b). For example, it decreases from ~0.41 ohm·m at the base of MTD 13 to ~0.39 ohm·m in undeformed strata below. The average resistivity of MTD 13 is ~0.33 ohm·m, ranging from ~0.21 ohm·m to ~0.47 ohm·m; i.e. ~65% higher than that of undeformed strata above (~0.20 ohm·m in the 5.3 m-thick interval to the sea floor). However, it is ~25% lower than the resistivity of undeformed strata below MTD 13 (~0.44 ohm·m within a ~20 m interval).

In terms of density, MTD 13 shows similar trends to MTD 11 and MTD 12 (Fig. 6c). It shows a sharp increase in density from ~1.50 g/cm^2 in undeformed strata above, to ~1.65 g/cm^2 at the top of MTD 12. At the base of MTD 13, the density decreases from ~1.99 g/cm^2 to ~1.92 g/cm^2. In general, the density of MTD 13 ranges from ~1.65 g/cm^2 to ~2.02 g/cm^2, for an average of ~1.85 g/cm^2. This average value is ~23.3% higher than for undeformed strata above MTD 13 (~1.5 g/cm^2 in the 5.3 m-thick interval to the sea floor).

3.3.4. Trendlines of MTDs and undeformed strata in the Amazon Fan

Three ODP sites (ODP Sites 933, 936 and 941) in the Amazon Fan show some typical differences (trendlines) between fine-grained MTDs and undeformed strata (Fig. 6).

The densities of MTDs and undeformed strata from the three sites show well-fitted logarithm relationships; R^2 = 0.76 for undeformed strata and R^2 = 0.80 for MTDs, respectively (Fig. 6c). However, the calculated best-fit curves suggest that the density of MTDs is larger than undeformed strata, with this difference becoming more pronounced with depth (Fig. 6c).

Regarding porosity, MTDs and undeformed strata also show a well-fitted logarithm relationship; R^2 = 0.73 for undeformed strata and R^2 = 0.85 for MTDs (Fig. 6c). Similarly to the density trend, the difference between the porosity of MTDs and undeformed strata becomes more pronounced with depth (Fig. 6c). The best-fit curves suggest that the porosity is always lower in MTDs than in undeformed strata (Fig. 6c).

Compared to density and porosity, the best-fit resistivity curves differ for MTDs and undeformed strata (Fig. 6b). In shallow strata (<100 mbsf), the resistivity of MTDs is lower than undeformed strata. However, the opposite occurs in strata deeper than 100 mbsf. In general, the resistivities of MTDs and undeformed strata have well-fitted logarithm curves; R^2 = 0.60 for undeformed strata and R^2 = 0.80 for MTDs (Fig. 6b).

3.5. Shear strength of MTDs

The shear strength of strata drilled at IODP Sites 1322 and 1324 in the Gulf of Mexico is highly variable, increasing gradually with depth (Fig. 7a). When considering MTD 1 and MTD 2 at IODP Site 1322, shear strength quickly increases from their top to their base, with maxima in shear strength recorded at their bases (Fig. 7a). Shear strength usually decreases sharply from the bases of MTDs into undeformed strata, e.g. shear strength drops from ~86.3 kPa to ~48.4 kPa at the base of MTD 2 (Fig. 7a). In MTD 7 at IODP Site 1324, shear strength increases from the top of MTD 7 to undeformed strata below. In general, the shear strengths of MTDs and undeformed strata at IODP Sites 1322 and 1324 show linear trends (Fig. 7a). The shear strength of undeformed strata is well-fitted with a R^2 = 0.71. However, the shear strength of MTDs

only shows a tentative linear relationship (R^2 =0.30) (Fig. 7a). The trends in shear strength are usually higher in MTDs than in undeformed strata, but they tend to intersect at relatively shallow depths below the sea floor (Fig. 7a).

The shear strength of strata drilled at ODP Sites 933, 936 and 941 (Amazon Fan) is also highly variable, once again increasing gradually with depth (Fig. 7b). The shear strength of MTDs is usually higher than undeformed strata. For example, the average shear strength of MTD 11 (~59.1 kPa) is ~53.8% and ~31.4% higher than undeformed strata above (~38.4 kPa within a ~20 m interval) and below (~45.0 kPa within ~20 m interval) (Fig. 7b). Moreover, the shear strength usually varies sharply at the boundaries of MTDs with undeformed strata, showing greater shear strength than undeformed strata above and below. For example, shear strength drops from ~69.3 kPa at the base of MTD 12 to ~53.6 kPa in undeformed strata below (Fig. 7b). In general, both the shear strengths of MTDs and undeformed strata at ODP Sites 933, 936 and 941 show well-fitted linear relationships (Fig. 7b). Importantly, the fitted curves of shear strength diverge with depth, with the MTDs' best-fit curve being always above that of undeformed strata (Fig. 7b).

3.6. Water content in MTDs

The water content of ODP Sites 933, 936 and 941 in the Amazon Fan is addressed in this section. Water content generally decreases with depth, revealing sharp variations when crossing the boundaries of MTDs into undeformed strata (Fig. 8). Water content decreases from ~28.9% in undeformed strata above MTD 12 to ~23.9% within this

mass-transport deposit. It decreases from ~52.6% in undeformed strata above to ~40.2% at the top of MTD 13. In contrast, water content usually sharply increases from the MTDs *per se* into undeformed strata below (Fig. 8). For example, they increase from ~23.2% and ~19.8% at the base of MTD 11 and MTD 12 to ~34.0% and ~23.9% in undeformed strata below, respectively. The average water content of MTD 11 (~24.1%) is ~18.6% and ~19.4%, lower than those of undeformed strata above (average of ~29.6% within a ~20 m interval) and below (average of ~29.9% within a ~20 m interval). The average water content of MTD 12 is ~22.7%, ranging from ~19.4% to 30.2%. It is ~27.0% and ~4.6% lower than those of undeformed strata above (average of ~31.1% within a ~10 m-thick interval) and below (average of ~23.8% in a ~10 m-thick interval).

MTD 13 has an average water content of ~31.2%, ranging from ~22.9% to ~40.4%; a value that is ~40.2% lower than that recorded by undeformed strata above (average of ~52.2% within a 5.3 m interval) and ~13.5% lower than that of undeformed strata below (average of 27.5% within a 10 m interval). Water contents for MTDs and undeformed strata show well-fitted logarithm relationships; R^2 = ~0.92 for undeformed strata and R^2 = ~0.87 for MTDs (Fig. 8). In addition, the water content curve for undeformed strata is always above that of MTDs, and this difference is kept constant at depth (Fig. 8).

3.7. Petrophysical properties of the main bodies and basal shear zones of MTDs

According to the trends of wireline curves, MTDs can be subdivided into two parts: their main bodies (the upper parts of MTDs) and their basal shear zones (the lowermost

parts of MTDs) (Figs. 2-5). These two distinctive parts show opposite trends on wireline data. For example, resistivity, bulk density and p-wave velocity (Vp) sharply decrease at the basal shear zone, when compared to main body of MTD (Figs. 2-5). Porosity greatly increases at the basal shear zone, contrasting to the relatively lower porosity documented in the main body of MTD (Figs. 2-5).

The average resistivity of the main body and basal shear zone of MTD shows a linear correlation (R^2 = ~0.54; Fig. 9a). Moreover, most of the average resistivity of basal shear zone (75%) is higher than that of the main body of MTD (Fig. 9a; Table 2). In contrast, there are no major differences between the average gamma-ray of the main MTD bodies and their basal shear zones (Fig. 9b; Table 2). The R^2 value of ~0.92 estimated for gamma-ray indicates a near-perfect linear relationship (Fig. 9b).

The average density of basal shear zones is lower than those in the main MTD bodies, with a R^2 value of ~0.64 (Fig. 9c; Table 2). In contrast to the average density, the average porosity of basal shear zones is higher than those in the main MTD bodies (Table 2), and it has a relatively moderate R^2 value of around 0.45 (Fig. 9d). Though the maximum thickness of basal shear zones can reach up to ~10.5 m (MTD 2), most (75%) are markedly thin, ranging in thickness between ~2.7 m and ~5.0 m (Fig. 9e; Table 2). The main bodies of MTDs are usually 2 to 19 times thicker than the basal shear zones (see also Alves and Lourenço, 2010) (Fig. 9e). The total thickness of MTDs also shows a partial correlation with the thicknesses of basal shear zones (R^2 = ~0.42; Fig. 9f).

4. Discussion

4.1. Factors influencing the petrophysical properties of MTDs

Through the detailed analysis of petrophysical data from fine-grained MTDs in the Gulf of Mexico, Ulleung Basin and Amazon Fan, and from MTDs samples by previous work (e.g. Piper et al., 1997; Sawyer et al., 2007, 2009; Dugan, 2012; Riedel et al., 2012; Reece et al., 2012), several key properties were recognised. They include:

(1) Resistivity, bulk density and p-wave velocity (Vp) usually increase at the top of MTDs, but decreasing sharply at their bases;

(2) Average resistivity is much higher in MTDs than that in undeformed strata confining these former deposits (Figs. 2-5; Table 1);

(3) Gamma-ray values show variable patterns in distinct MTDs, with no clear trends observed between MTDs and undeformed strata (Figs. 2-5);

(4) Porosity usually drops at the top of MTDs to increase at their bases, showing a reverse trend to bulk density (Figs. 2-5, 10);

(5) The average porosity of MTDs is usually lower than the porosity of undeformed strata directly above and below (Figs. 2-5);

(6) The shear strength of MTDs increases from their tops to their bases, and is usually higher than the shear strength of undeformed strata above and below (Figs. 7, 10);

(7) Water content in MTDs is much lower than that in undeformed strata, with sharp variations observed at the top and base of MTDs (Fig. 8).

Apart from these common characteristics, we also observe that the petrophysical character of basal shear zones of MTDs have opposite trends to their main bodies, i.e. increasing porosities and decreasing resistivity, bulk density and velocity (Figs. 2-5, 10).

Gamma-ray values are mainly controlled by lithology. As the studied MTDs are mainly composed of mud-dominated sediment of similar composition to 'background' slope strata, there are no sharp increases or decreases in gamma-ray values between MTDs and their confining undeformed intervals (Figs. 2-5, 10).

Resistivity, bulk density, velocity and porosity indicate that the MTDs are more consolidated than background sediment, as also reported by many previous studies (e.g. Piper et al., 1997; Shipp et al., 2004; Strasser et al., 2011; Dugan, 2012; Sun et al., 2018) (Fig. 10). Apart from overburden stress, failed sediment is also subjected to shear stress during its emplacement (Fig. 10), partly justifying the observed over-consolidation of the studied MTDs (Figs. 2-6). This additional source of shear stress results in a reduction in porosity, with consequent dewatering of failed strata. Dewatering would also result in relative increases in density and Vp values, as observed in this study; resistivity is more sensitive to the loss of water in mud-dominated sediments, and thus sharp variations can be observed at the tops and bases of MTDs (Fig. 10).

Opposite trends to the latter are observed when comparing the basal shear zones with the main bodies of MTDs, suggesting that the consolidation of strata in basal shear zones is relatively moderate. This characteristic is likely caused by extreme shearing at

the base of MTDs to form shear fractures and pervasive fabric in their basal shear zones (Alves and Lourenço, 2010; Alves, 2015; Cardona et al., 2016) (Fig. 10). The shear stress always increases from the tops of the MTDs to their bases (e.g. Piper et al., 1997; De Blasio et al., 2004), because of the relative movement (friction) experienced by failed sediment, and also between the failed sediment and undeformed strata below. Such an observation is supported by the wireline curve shapes in the MTDs, particularly by the gradual increase in resistivity recorded in them (Figs. 2-6). When the shear stress exceeds the shear strength of inclined strata on a continental slope, at the critical point for shear failure, fractures would form within the soon-to-be basal shear zone, as corroborated by: (1) the larger shear stress limits of strata at the base of MTDs (Fig. 7), and (2) the widespread occurrence of fractures at the base of MTDs in cores and FMI (resistivity image logging) data from the Ulleung Basin (Riedel et al., 2012), Nankai Trough (Expedition 333 Scientists, 2011), Amazon Fan (Piper et al., 1997) and eastern North American margin (Tripsanas et al., 2008). In the Ulleung Basin, fractures are also perpendicular to the seismically defined flow-path of MTD 9 (Riedel et al., 2012), suggesting they were caused by significant shearing during its emplacement.

4.2. MTDs and fluid flow

Based on the low water contents of MTDs (Fig. 8) and the abundant fluid flow structures in them, we postulate a large volume loss of fluid during MTD emplacement (Piper et al., 1997; Shipp et al., 2004; Strasser et al., 2011). The over-consolidation of MTDs during their emplacement (and burial) not only results in the loss of porosity, but

also causes a relative reduction in permeability. For example, MTDs at IODP Sites U1324 (MTD 7) and U1322 (MTD 2) in the Gulf of Mexico show reductions in permeability in the order of ~33% and ~71% with respect to normally-consolidated mud above and below (Dugan, 2012). Porosity and permeability losses in MTDs greatly increase their seal competence, a character indicating that they generally comprise seal intervals and hinder vertical fluid flow after their emplacement (e.g. Shipp et al., 2004; Reece et al., 2012; Alves et al., 2014; Hornbach et al., 2015; Sun et al., 2017, 2018) (Fig. 10).

Compared to the main body of the MTDs, the basal shear zone has a distinctive role in controlling fluid flow (Fig. 10). Due to the occurrence of highly porous zones (e.g. fractured strata), fluid can accumulate within or migrate upslope along basal shear zones (e.g, Alves and Lourenço, 2010; Sun et al., 2017). This is the main reason why fluid seepage and cold-water carbonates are usually observed at the headwall scarps of MTDs, such as in the case of the Eivissa Channel of western Mediterranean Sea (Lastras et al., 2004), Amazon Fan (Dano et al., 2014), north Sicily continental margin (Pennino et al., 2014) and Great Bahama Bank (Principaud et al., 2015). The latest observations from the South China Sea show that free gas accumulates at the bases of MTDs, confirming their basal shear zones are relatively porous (Sun et al., 2017).

4.3. Implications to the recurrent triggering of submarine landslides

Submarine slope instability is a theme widely studied, and phenomena such as earthquakes (e.g. Moscardelli et al., 2006), high sedimentation rates (e.g. Dalla Valle et

al., 2013; Noda et al., 2013), gas hydrate dissolution (e.g. Laberg and Vorren, 2000; Maslin et al., 2005), sea-level variations (e.g. Smith et al., 2013; Urlaub et al., 2013), and tectonic activity (e.g. Chadwick et al., 2012; Laberg et al., 2014), have been proposed in the literatures as capable of triggering large landslides. However, one is not entirely sure of the factors triggering slope failures in most documented cases of submarine slope instability. In particular, there is significant less knowledge about the critical conditions under which a slope failure will occur. Most published data concerns ancient slope failures, with their formation mechanisms and triggers being hard to estimate. In addition, it is difficult to predict when and where a slope failure will occur in the future, and there is an overall lack of *in-situ* measurements in the areas where recent submarine landslides have occurred.

This study suggests that slope sediments can fail under their own gravity when gravitational forces along the slope overcome the shear strength of sediments. This failure mechanism does not require other triggers, such as earthquakes, gas hydrate dissolution and sea-level fluctuations, and is likely responsible for some of the frequent submarine slope failures at the steep slopes, such as offshore northern Norway where muddy contourites failed along the surfaces between them and coarse-grained turbidites on a steep continental slope (Laberg et al., 2016) (Fig. 11). Accompanying this increase in sediment thickness, fractures would occur in slope strata in response to increasing shear stress (Figs. 10, 11b). Fluids in-situ or in adjacent intervals could migrate into these fractures, decreasing the shear strength of slope strata to form a weak layer (Fig. 11b). Under the effect of fluids and the subsequent formation of the weak layer,

overlying strata will fail and slope failure will occur in a process similar to the pressure-driven slope failure reported in Flemings et al. (2008), Shillington et al. (2012), Le Friant et al. (2015) and Hornbach et al. (2015) (Fig. 11c). Fluids can migrate laterally along the basal shear zone, to finally escape from the extensional headwall zone (Fig. 11c), as documented in the Eivissa Channel of the western Mediterranean Sea (Lastras et al., 2004).

This study also suggests that the main bodies of MTDs can generate important overpressure below them, with unexpected high pore pressures being likely encountered during drilling. Such overpressures have been documented under MTDs in the Gulf of Mexico (Sawyer et al., 2009; Reece et al., 2012) and the Islands of Montserrat and Martinique in the Caribbean Sea (Hornbach et al., 2015). Furthermore, the lateral migration of fluids, especially along the basal shear zone, may trigger new slope instability in shallow strata to form regressive slope failures, as reported in the South China Sea (Sun et al., 2017).

5. Conclusions

Through the detailedly qualitative and quantitative analysis of well-log data from IODP/ODP Sites and one exploration well, we find that the main bodies of MTDs generally have similar geophysical properties to those indicated in previous studies. However, we identify some new characteristics and trends that are important for the analysis of MTDs as potential geohazards. The main results of this work are as follows:

1. When compared to undeformed strata above and below, the main bodies of MTDs are typically characterized by their higher resistivity, velocity, bulk density and shear strength, plus their lower porosity, water content and permeability;
2. The main bodies of MTDs are more consolidated than undeformed strata above and below, probably a character resulting from dewatering and shear compaction during MTD emplacement;
3. The petrophysical character of the lowermost parts of MTDs (basal shear zones) are the opposite (i.e. they show lower resistivity, velocity, bulk density and higher porosity) from the main bodies of MTDs. This difference is likely attributed to the presence of fractures in basal shear zones caused by excessive shear stress;
4. The main bodies of MTDs could serve as good seal units after their emplacement to hinder vertical fluid migration. However, fluids could accumulate or laterally migrate along fractured basal shear zones;
5. Inclined sediments can fail under their own gravity without any triggers (e.g. earthquakes) with fractured zones, possibly charged by fluid, acting as weak layers. In addition, fractured basal shear zone with high pore pressure represents an important geohazard when drilling.

Acknowledgments

This research supported by the National Scientific Foundation of China (Grant Nos. 41676051 and 41372112), the Programme of Introducing Talents of Discipline to Universities (No. B14031), the Fundamental Research Funds for the Central

Universities-the China University of Geosciences (Wuhan) (No. CUG160604) and the China Scholarship Council (201906415013). This work benefited from the dedication and efforts of the participants and technical staff of ODP Expedition 155 and IODP Expedition 308. Finally, we thank Editor Michel Faure and an anonymous reviewer for their constructive comments on this manuscript.

References

Alves, T.M., 2015. Submarine slide blocks and associated soft-sediment deformation in deep-water basins: A review. *Marine and Petroleum Geology, 67*, 262-285, https://doi.org/10.1016/j.marpetgeo.2015.05.010.

Alves, T.M., Kurtev, K., Moore, G.F., Strasser, M., 2014. Assessing the internal character, reservoir potential, and seal competence of mass-transport deposits using seismic texture: A geophysical and petrophysical approach. *AAPG Bulletin, 98*, 793-824, https://doi.org/10.1306/09121313117.

Alves, T.M., Lourenco, S., 2010. Geomorphologic features related to gravitational collapse: submarine landsliding to lateral spreading on a Late Miocene-Quaternary slope (SE Crete, eastern Mediterranean). *Geomorphology, 123*, 13-33, https://doi.org/10.1016/j.geomorph.2010.04.030.

Bahk, J.J., Kang, N.K., Yi, B.Y., Lee, S.H., Jeong, S.W., Urgeles, R., Yoo, D.G., 2017. Sedimentary characteristics and processes of submarine mass-transport deposits in the Ulleung Basin and their relations to seismic and sediment physical properties. *Marine Geology, 393*, 124-140, http://dx.doi.org/10.1016/j.margeo.2017.05.010.

Bull, S., Cartwright, J., Huuse, M., 2009. A review of kinematic indicators from mass-transport complexes using 3D seismic data. *Marine and Petroleum Geology, 26*, 1132-1151, https://doi.org/10.1016/j.marpetgeo.2008.09.011.

Bünz, S., Mienert, J., Bryn, P., Berg, K., 2005. Fluid flow impact on slope failure from 3D seismic data: A case study in the Storegga Slide. *Basin Research, 17*, 109-122, https://doi.org/10.1111/j.1365-2117.2005.00256.x.

Chadwick, W., Dziak, R., Haxel, J., Embley, R., Matsumoto, H., 2012. Submarine landslide triggered by volcanic eruption recorded by in situ hydrophone. *Geology, 40*, 51-54, https://doi.org/10.1130/G32495.1.

Dalla Valle, G., Gamberi, F., Rocchini, P., Minisini, D., Errera, A., Baglioni, L., Trincardi, F., 2013. 3D seismic geomorphology of mass transport complexes in a foredeep basin: examples from the Pleistocene of the Central Adriatic Basin (Mediterranean Sea). *Sedimentary Geology, 294*, 127-141, https://doi.org/10.1016/j.sedgeo.2013.05.012.

Dano, A., Praeg, D., Migeon, S., Augustin, J.M., Ceramicola, S., Ketzer, J., Augustin, A.H., Ducassou, E., Mascle, J., 2014. Fluid Seepage in Relation to Seabed Deformation on the Central Nile Deep-Sea Fan, Part 1: Evidence from Sidescan Sonar Data, In: Krastel, S., et al. eds., Submarine Mass Movements and Their Consequences, Advances in Natural and Technological Hazards Research, 37, 129-139, https://doi.org/10.1007/978-3-319-00972-8 12.

Dugan, B., 2012. Petrophysical and consolidation behavior of mass-transport deposits from the northern Gulf of Mexico, IODP Expedition. *Marine Geology, 315-318*, 98-

107, https://doi.org/10.1016/j.margeo.2012.05.001.

Expedition 308 Scientists., 2005. Overpressure and fluid flow processes in the deepwater Gulf of Mexico: slope stability, seeps, and shallow-water flow: IODP Preliminary Report, 308, https://doi.org/10:2204/iodp.pr.308.2005

Expedition 333 Scientists., 2011. NanTroSEIZE Stage 2: subduction inputs 2 and heat flow. IODP Preliminary Report, 333, https://doi.org/10.2204/iodp.pr.333.2011.

Flemings, P. B., Behrmann, I., Davies, T., John, C., the Expedition 308 Project Team., 2005. Gulf of Mexico hydrogeology-Overpressure and fluid flow processes in the deepwater Gulf of Mexico: Slope stability, seeps, and shallow-water flow: IODP Scientific Prospects, https://doi.org/30810.2204/iodp.sp.308.

Flemings, P.B., Long, H., Dugan, B., Germaine, J., John, C., Behrmann, J.H., Sawyer, D., Scientists, I.E., 2008. Pore pressure penetrometers document high overpressure near the seafloor where multiple submarine landslides have occurred on the continental slope, offshore Louisiana, Gulf of Mexico. *Earth Planetary Science Letters, 269*, 309-324, https://doi.org/10.1016/j.epsl.2007.12.005.

Frey-Martínez, J., Cartwright, J., Hall, B., 2005. 3D seismic interpretation of slump complexes: examples from the continental margin of Israel. *Basin Research, 17*, 83-108, https://doi.org/10.1111/j.1365-2117.2005.00255.x.

Fu, Y.Z., von Dobeneck, T., Franke, C., Heslop, D., Kasten, S., 2008. Rock magnetic identification and geochemical process models of greigite formation in Quaternary marine sediments from the Gulf of Mexico (IODP Hole U1319A). *Earth and Plantary Science Letters, 275*, 233-245, https://doi.org/10.1016/j.epsl.2008.07.034.

Cardona, S., Wood, L.J., Day-Stirrat, R.J., Moscardelli, L., 2016. Fabric Development and Pore-Throat Reduction in a Mass-Transport Deposit in the Jubilee Gas Field, Eastern Gulf of Mexico: Consequences for the Sealing Capacity of MTDs. In: Lamarche G. et al. (eds) Submarine Mass Movements and their Consequences. Advances in Natural and Technological Hazards Research, Springer, Cham, 41, https://doi.org/10.1007/978-3-319-20979-1_3.

Gee, M.J.R., Gawthorpe, R.L., Friedmann, S.J., 2006. Triggering and evolution of a giant landslide, offshore Angola revealed by 3D seismic stratigraphy and geomorphology. *Journal of Sedimentary Research, 76*, 9-19, https://doi.org/10.2110/jsr.2006.02.

Gong, C.L., Wang, Y.M., Hodgson, D.M., Zhu, W.L., Li, W.G., Xu, Q., Li, D., 2014. Origin and anatomy of two different types of mass transport complexes: A 3D seismic case study from the northern South China Sea margin. *Marine and Petroleum Geology, 54*, 198-215, https://doi.org/10.1016/j.marpetgeo.2014.03.006.

Hornbach, M.J., Manga, M., Genecov, M., Valdez, R., Miller, P., Saffer, D., Adelstein, E., Lafuerza, S., Adachi, T., Breitkreuz, C., Jutzeler, M., Le Friant, A., Ishizuka, O., Morgan, S., Slagle, A., Talling, P.J., Fraass, A., Watt, S. F.L., Stroncik, N.A., Aljahdali, M., Boudon, G., Fujinawa, A., Hatfield, R., Kataoka, K., Maeno, F., Martinez-Colon, M., McCanta, M., Palmer, M., Stinton, A., Subramanyam, K.S.V., Tamura, Y., Villemant, B., Wall-Palmer, D., Wang, F., 2015. Permeability and pressure measurements in Lesser Antilles submarine slides: Evidence for pressure-driven slow-slip failure. *Journal of Geophysical Research: Solid Earth, 120,* 7986-

8011, https://doi.org/10.1002/2015JB012061.

Judd, A.G., Hovland, M., 2007. Seabed fluid flow: the impact on Geology, Biology and the Marine Environmen. Cambridge University Press, Cambridge.

Krastel, S., Wynn, R.B., Hanebuth, T.J.J., Henrich, R., Holz, C., Meggers, H., Kuhlmann, H., Georgiopoulou, A., Schulz, H.D., 2006. Mapping of seabed morphology and shallow sediment structure of the Mauritania continental margin, Northwest Africa: some implications for geohazard potential. *Norwegian Journal of Geology, 86*, 163-176, https://doi.org/10.1016/j.asr.2005.07.022

Laberg, J.S., Baeten, N.J., Vanneste, M., Forsberg, C.F., Forwick, M., Haflidason, H., 2016. Sediment failure affecting muddy contourites on the continental slope offshore northern Norway: Lessons learned and some outstanding issues. In: Lamarche ,G. et al. (eds) Submarine Mass Movements and their Consequences. Advances in Natural and Technological Hazards Research, Springer, Cham, 41, 281-289, https://doi.org/10.1007/978-3-319-20979-1_28.

Laberg, J.S., Vorren, T.O., 2000. The Trænadjupet Slide, offshore Norway morphology, evacuation and triggering mechanisms. *Marine Geology, 171*, 95-114, https://doi.org/10.1016/S0025-3227(00)00112-2.

Laberg, J.S., Kawamura, K., Amundsen, H., Baeten, N., Forwick, M., Rydningen, T.A., Vorren, T.O., 2014. A submarine landslide complex affecting the Jan Mayen Ridge, Norwegian Greenland Sea: slide scar morphology and processes of sediment evacuation. *Geo-Marine Letter, 34*, 51-58, https://doi.org/10.1007/s00367-013-0345-z.

Lastras, G., Canals, M., Urgeles, R., Hughes-Clarke, J.E., Acosta, J., 2004. Shallow slides and pockmark swarms in the Eivissa Channel, western Mediterranean Sea. *Sedimentology, 51*, 837-850, https://doi.org/10.1111/j.1365-3091.2004.00654.x.

Lee, S., Stow, D.V., 2007. Laterally contiguous, concave-up basal shear surfaces of submarine landslide deposits (Miocene), southern Cyprus: differential movement of sub-blocks within a single submarine landslide lobe. *Geosciences Journal, 11*, 315-321, https://doi.org/10.1007/BF02857048.

Le Friant, A., Ishizuka, O., Boudon, G., Palmer, M.R., Talling, P.J., Villemant, B., Adachi, T., Aljahdali, M., Breitkreuz, C., Brunet, M., Caron, B., Coussens, M., Deplus, C., Endo, D., Feuillet, N., Fraas, A.J., Fujinawa, A., Hart, M.B., Hatfield, R.J., Hornbach, M., Jutzeler, M., Kataoka, K.S., Komorowski, J.-C., Lebas, E., Lafuerza, S., Maeno, F., Manga, M., Martínez‐Colón, M., McCanta, M., Morgan, S., Saito, T., Slagle, A., Sparks, S., Stinton, A., Stroncik, N., Subramanyam, K.S.V., Tamura, Y., Trofimovs, J., Voight, B., Wall-Palmer, D., Wang, F., Watt, S.F.L., 2015. Submarine record of volcanic island construction and collapse in the Lesser Antilles arc: First scientific drilling of submarine volcanic island landslides by IODP Expedition 340. *Geochemistry Geophysics Geosystem, 16*, 420-442, https://doi.org/10.1002/2014GC005652.

Li, W., Alves T.M., Wu, S.G., Völker, D., Zhao, F., Mi, L.J., Kopf, A., 2015. Recurrent slope failure and submarine channel incision as key factors controlling reservoir potential in the South China Sea (Qiongdongnan Basin, South Hainan Island). *Marine and Petroleum Geology, 64*, 17-30,

https://doi.org/10.1016/j.marpetgeo.2015.02.043.

Locat, J., Lee, H.J., 2002. Submarine landslides: advances and challenges. *Canadian Geotechnical Journal, 39*, 193-212, https://doi.org/10.1139/t01-089.

Long, H., Flemings, P.B., Germaine, J.T., Saffer, D.M., 2011. Consolidation and overpressure near the seafloor in the Ursa Basin, Deepwater Gulf of Mexico. *Earth and Planetary Science Letters, 305*, 11-20, https://doi.org/10.1016/j.epsl.2011.02.007.

Maslin, M., Vilela, C., Mikkelsen, N., Grootes, P., 2005. Causes of catastrophic sediment failures of the Amazon Fan. *Quaternary Science Reviews, 24*, 2180-2193, https://doi.org/10.1016/j.quascirev.2005.01.016.

Masson, D.G., Harbitz, C.B., Wynn, R.B., Pedersen, G., Lovholt, F., 2006. Submarine landslides: processes, triggers and hazard prediction: Philosophical Transactions. *Series A, Mathematical, Physical, and Engineering Sciences, 364*, 2009-2039, https://doi.org/10.1098/rsta.2006.1810.

McAdoo, B.G., Pratson, L.F., Orange, D.L., 2000. Submarine landslide geomorphology, U.S. Continental slope. *Marine Geology, 169*, 103-136, doi: 10.1016/S0025-3227(00)00050-5.

Moscardelli, L., Wood, L., 2008. New classification system for mass-transport complexes in offshore Trinidad. *Basin Research, 20*, 73-98, https://doi.org/10.1111/j.1365-2117.2007.00340.x.

Moscardelli, L., Wood, L., Mann, P., 2006. Mass-transport complexes and associated processes in the offshore area of Trinidad and Venezuela. *AAPG Bulletin, 90*, 1059-

1088, https://doi.org/10.1306/02210605052.

Noda, A., TuZino, T., Joshima, M., Goto, S., 2013. Mass transport-dominated sedimentation in a foreland basin, the Hidaka Trough, northern Japan. *Geochemistry, Geophysics, Geosystems, 14*, 2638-2660, https://doi.org/10.1002/ggge.20169.

Patricia, L. M., Pirmez, C., Busch, W., Cramp, A., 1997. Grain-size characterization of Amazon Fan deposits and comparison to seismic facies units, in Flood, R.D., Piper, D.J.W., Klaus, A., and Peterson, L.C., eds., Proceedings of the Ocean Drilling Program, Scientific Results, 155, 35-52, https://doi.org/10.2973/odp.proc.sr.155.209.1997.

Paull, C.K., Brewer, P., Ussler, W., Peltzer, E., Rehder, G., Clague, D., 2003. An experiment demonstrating that marine slumping is a mechanism to transfer methane from seafloor gas-hydrate deposits into the upper ocean and atmosphere. *Geo-Marine Letters, 22*, 198-203, https://doi.org/10.1007/s00367-002-0113-y.

Pennino, V., Sulli, A., Caracausi, A., Grassa, F., Interbartolo, F., 2014. Fluid escape structures in the north Sicily continental margin. *Marine and Petroleum Geology, 55*, 202-213, https://doi.org/10.1016/j.marpetgeo.2014.02.007.

Piper, D.J.W., Pirmez, C., Manley, P.L., Long, D., Food, R.D., Normark, W.R., Showers, W., 1997. Mass-transport Deposits of the Amazon Fan, in Flood, R.D., Piper, D.J.W., Klaus, A., and Peterson, L.C., eds., Proceedings of the Ocean Drilling Program, Scientific Results, 155, 109-146, https://doi.org/10.2973/odp.proc.sr.155.212.199.

Pirmez, C., Flood, R.D., Baptiste, J., Yin, H.Z., Manley, P.L., 1997. Clay content, porosity and velocity of Amazon Fan sediments determined from ODP Leg 155 cores

and wireline logs. *Geophysical Research Letters, 24*, 317-320, https://doi.org/1029/96GL03469.

Posamentier, H., 2004. Stratigraphy and geomorphology of deep-water mass transport complexes based on 3D seismic data: Offshore Technology Conference, Houston, Texas, Extended Abstract, OTC16740, https://doi.org/10.4043/16740-MS.

Posamentier, H.W., Kolla, V., 2003. Seismic geomorphology and stratigraphy of depositional elements in deep-water settings. *Journal of Sedimentary Research, 73*, 367-388, https://doi.org/10.1306/111302730367.

Principaud, M., Mulder, T., Gillet, H., Borgomano, J., 2015. Large-scale carbonate submarine mass-wasting along the northwestern slope of the Great Bahama Bank (Bahamas): Morphology, architecture, and mechanisms. *Sedimentary Geology, 317*, 27-42, https://doi.org/10.1016/j.sedgeo.2014.10.008.

Reece, J.S., Flemings, P.B., Dugan, B., Long, H., Germaine, J.T., 2012. Permeability-porosity relationships of shallow mudstones in the Ursa Basin, northern deepwater Gulf of Mexico. *Journal of Geophysical Research, 117*, B12102, https://doi.org/10.1029/2012JB009438.

Riedel, M., Bahk, J.J., Scholz, N.A., Ryu, B.J., Yoo, D. G., Kim, W., Kim, G.Y., 2012. Mass-transport deposits and gas hydrate occurrences in the Ulleung Basin, East Sea e Part 2: Gas hydrate content and fracture-induced anisotropy. *Marine and Petroleum Geology, 35*, 75-90, https://doi.org/10.1016/j.marpetgeo.2012.03.005.

Sawyer, D.E., Flemings, P.B., Dugan, B., Germaine, J.T., 2009. Retrogressive failures recorded in mass-transport deposits in the Ursa Basin, Northern Gulf of Mexico.

Journal of Geophysical Research, 14, B10102, https://doi.org/10.1029/2008JB006159.

Sawyer, D.E., Flemings, P.B., Shipp, R.C., Winker, C.D., 2007. Seismic geomorphology, lithology, and evolution of the late-Pleistocene Mars-Ursa turbidite region, Mississippi Canyon area, northern Gulf of Mexico. *AAPG Bulletin, 91*, 215-234, https://doi.org/10.1306/08290605190.

Shillington, D.J., Seeber, L., Sorlien, C.C., Steckler, M.S., Kurt, H., Dondurur, D., Çifçi, G., İmren, C., Cormier, M.-H., McHugh, C.M.G., Gürçay, S., Poyraz, D., Okay, S., Atgın, O., Diebold J.B., 2012. Evidence for widespread creep on the flanks of the Sea of Marmara transform basin from marine geophysical data. *Geology, 40*, 439-442, https://doi.org/10.1130/G32652.1.

Shipp, R.C., Nott, J.A., Newlin, J.A., 2004. Physical characteristics and impact of mass transport complexes on deepwater jetted conductors and suction anchor piles: Offshore Technology Conference, Houston, Texas, Extended Abstract, OTC16751, https://doi.org/10.4043/16751-MS.

Smith, D.E., Harrison, S., Jordan, J.T., 2013. Sea level rise and submarine mass failures on open continental margins. *Quaternary Science Reviews, 82*, 93-103, https://doi.org/10.1016/j.quascirev.2013.10.012.

Strasser, M., Moore, G.F., Kimura, G., Kopf, A.J., Underwood, M.B., Guo, J.H., Screaton, E.J., 2011. Slumping and mass transport deposition in the Nankai fore arc: Evidence from IODP drilling and 3-D reflection seismic data. *Geochemistry, Geophysics, Geosystems, 12*, Q0AD13, https://doi.org/10.1029/2010GC003431.

Sultan, N., Cochonat, P., Canals, M., Cattaneo, A., Dennielou, B., Haflidason, H., Laberg, J.S., Long, D., Mienert, J., Trincardi, F., 2004. Triggering mechanisms of slope instability processes and sediment failures on continental margins: a geotechnical approach. *Marine Geology, 213*, 291-321, https://doi.org/10.1016/j.margeo.2004.10.011.

Sun, Q.L., Alves, T., Xie, N.N., He, J.X., Li, W., Ni, X.L., 2017. Free gas accumulations in basal shear zones of mass-transport deposits (Pearl River Mouth Basin, South China Sea): An important geohazard on continental slope basins. *Marine and Petroleum Geology, 81*, 17-32, https://doi.org/10.1016/j.marpetgeo.2016.12.029.

Sun, Q.L., Alves, T.M., Lu, X.Y., Chen, C. X., Xie, X.N., 2018. True volumes of slope failure estimated from a Quaternary mass-transport deposit in the northern South China Sea. *Geophysical Research Letters, 45*, 2642-2651, https://doi.org/10.1002/2017GL076484.

Tripsanas, E.K., Piper, D.J.W., Jenner, K.A., Bryant, W., 2008. Submarine mass-transport facies: new perspectives on flow processes from cores on the eastern North American margin. *Sedimentology, 55*, 97-136, https://doi.org/10.1111/j.1365-3091.2007.00894.x.

Urgeles, R., Locat, J., Sawyer, D.E., Flemings, P.B., Dugan, B., Binh, N.T.T., 2010. History of pore pressure build up and slope instability in mud-dominated sediments of Ursa Basin, Gulf of Mexico continental slope. In: Mosher, D.C; Shipp, R.C; Moscardelli, L; Chaytor, J.D; Baxter, C.D.P; Lee, H.J; Urgeles, R (Eds), Submarine Mass Movements and Their Consequences. Advances in Natural and Technological

Hazards Research, Springer, Dordrecht, 28, 179-190. https://doi.org/10.1007/978-90-481-3071-9_15.

Urlaub, M., Talling, P.J., Masson, D.G., 2013. Timing and frequency of large submarine landslides: implications for understanding triggers and future geohazard. *Quaternary Science Reviews, 72*, 63-82, https://doi.org/10.1016/j.quascirev.2013.04.020.

Weimer, P., 1989. Sequence stratigraphy of the Mississippi fan (Plio-Pleistocene), Gulf of Mexico. *Geo-Marine Letters, 9*, 185-272, https://doi.org/10.1007/BF02431072.

Figure captions

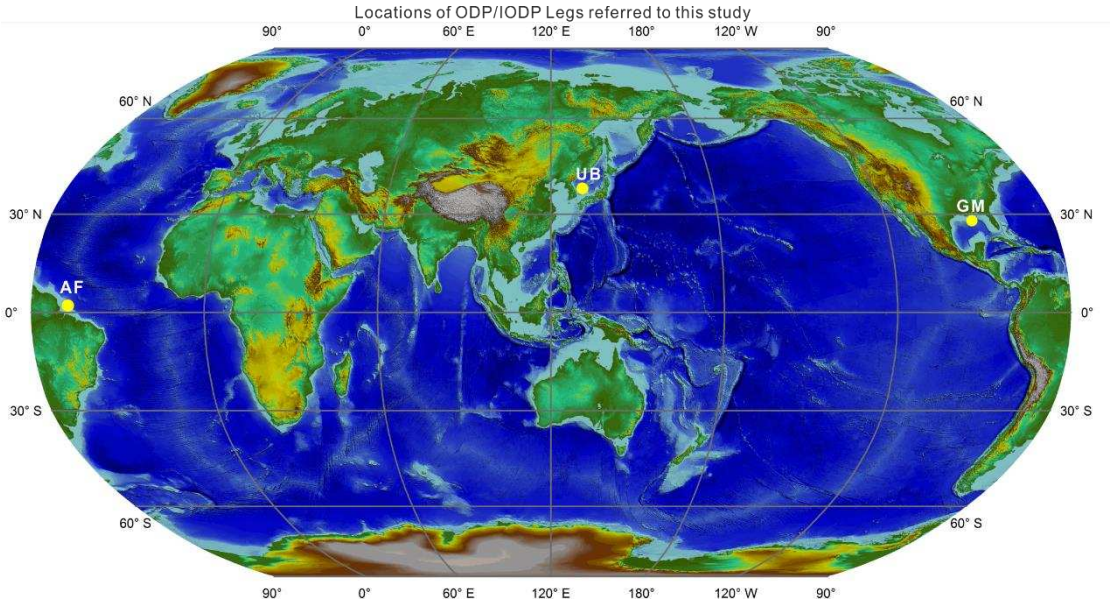

Figure 1: Locations of the representative mass-transport deposits (MTDs) analysed in this study. AF = Amazon Fan; GB = Gulf of Mexico; UB = Ulleung Basin.

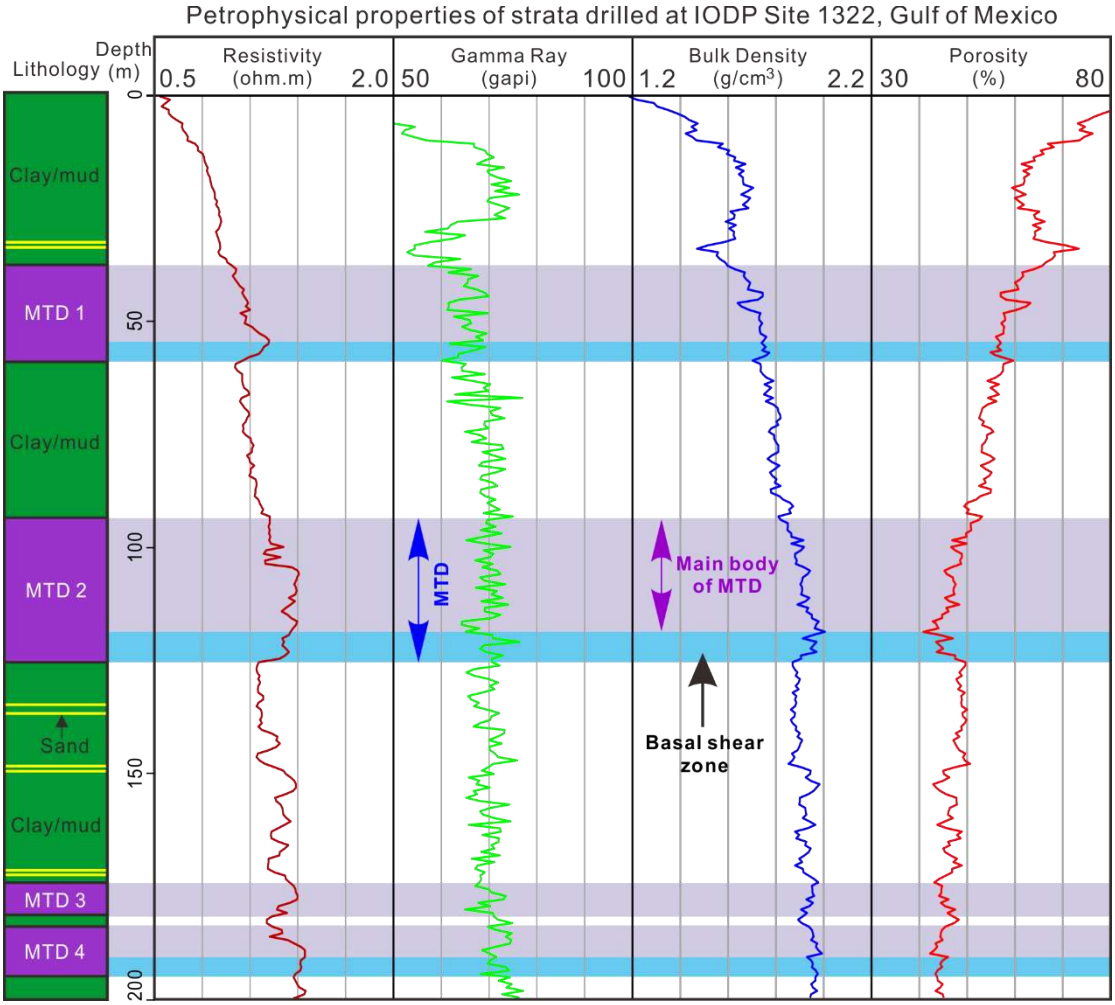

Figure 2: Petrophysical data for IODP Site U1322 (Expedition 308), Gulf of Mexico, showing borehole resistivity, gamma ray, bulk density and porosity in MTDs 1 to 4, and in undeformed slope strata. Lithological column is modified from Expedition 308 Scientists (2005).

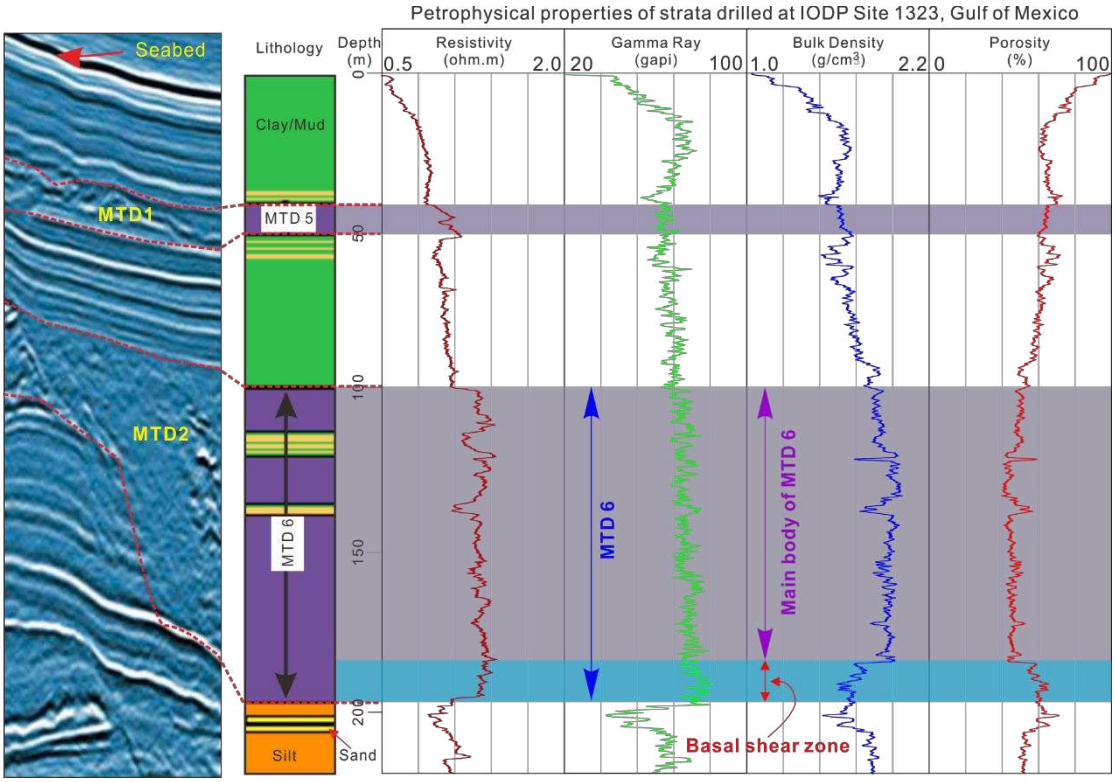

Figure 3: Petrophysical data for IODP Site U1323 (Expedition 308), Gulf of Mexico, showing borehole resistivity, gamma ray, bulk density and porosity in MTDs 5 and 6, and in undeformed slope strata. The seismic profile and lithological column are modified from Expedition 308 Scientists (2005).

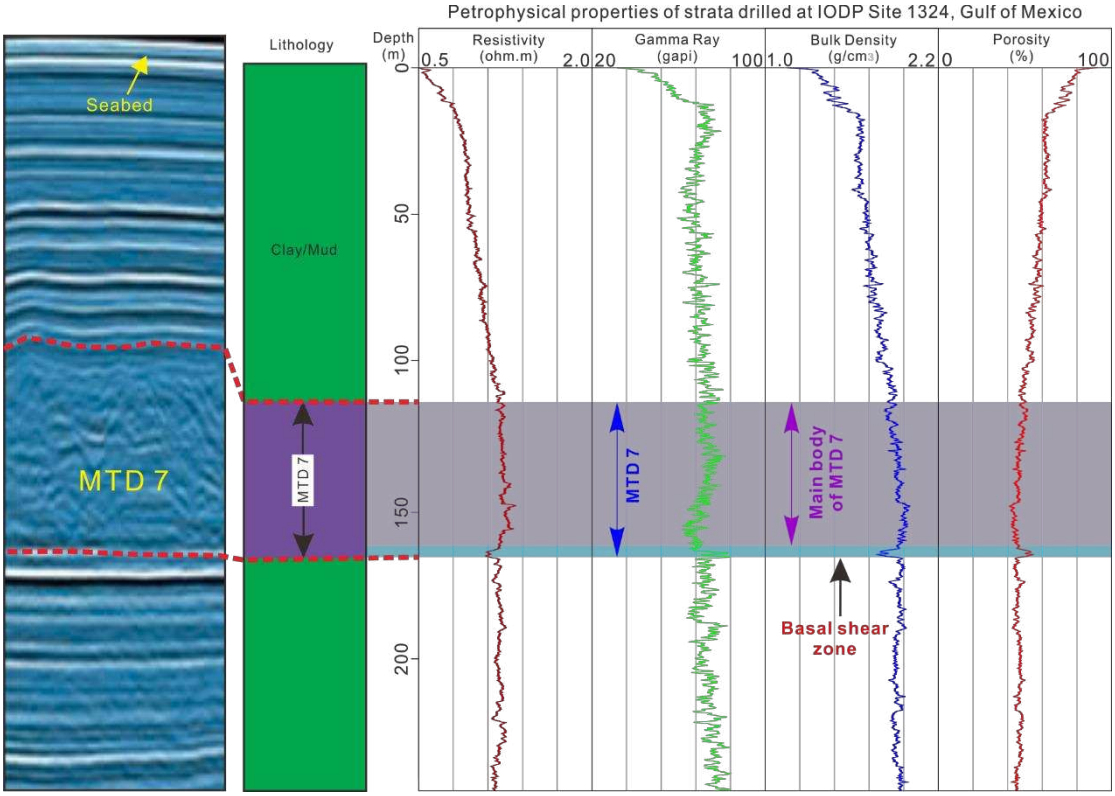

Figure 4: Petrophysical data for IODP Site U1324 (Expedition 308), Gulf of Mexico, showing borehole resistivity, gamma ray, bulk density and porosity in MTD 7 and in undeformed slope strata. Seismic profile and lithological column are modified from Expedition 308 Scientists (2005).

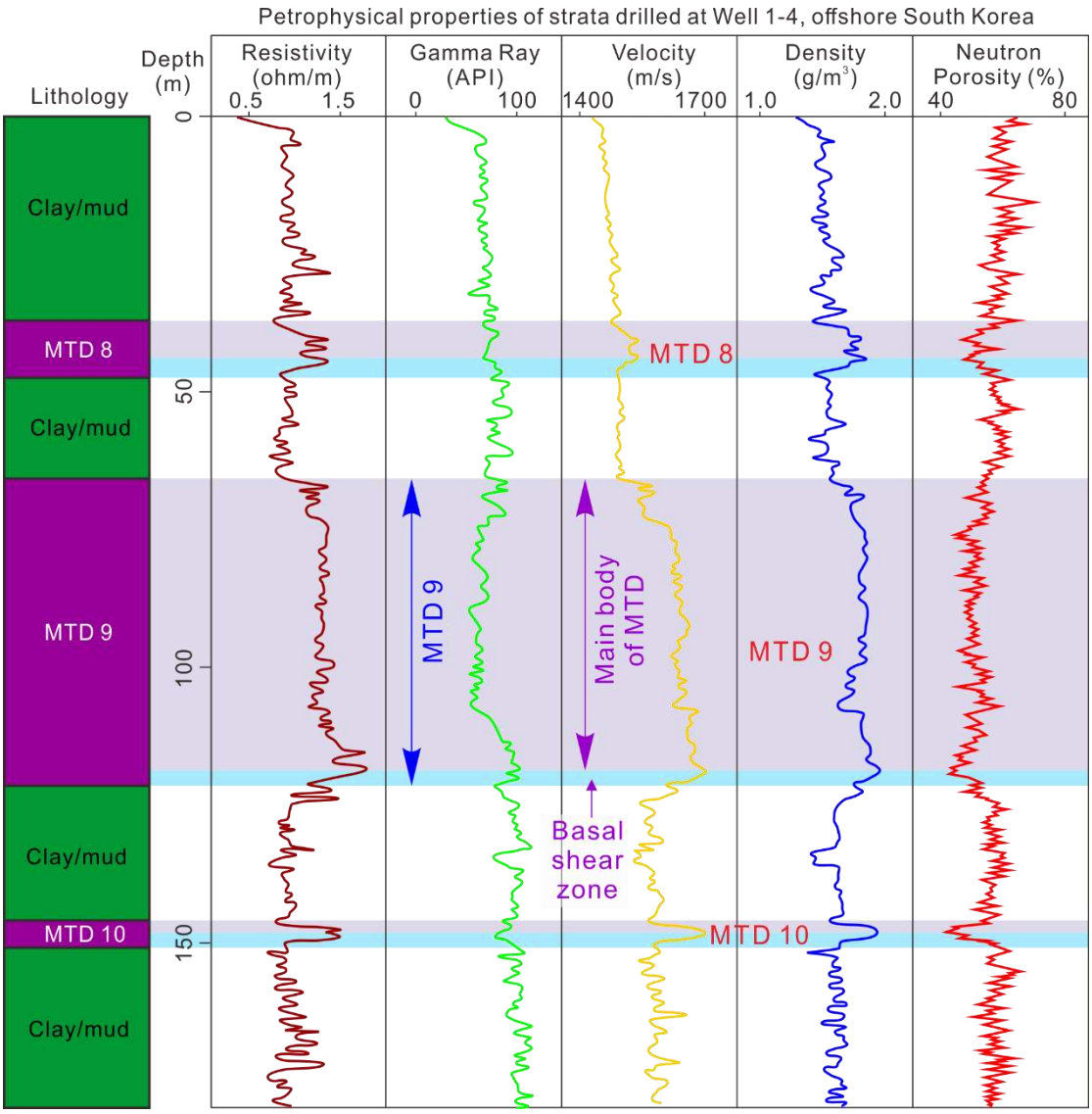

Figure 5: Petrophysical data for UBGH 1-4 in the Ulleung Basin (South Korea) showing borehole resistivity, gamma ray, compressional velocity, bulk density and neutron porosity in MTDs 8 to 10, and in undeformed slope strata. Figure is modified from Riedel et al. (2012).

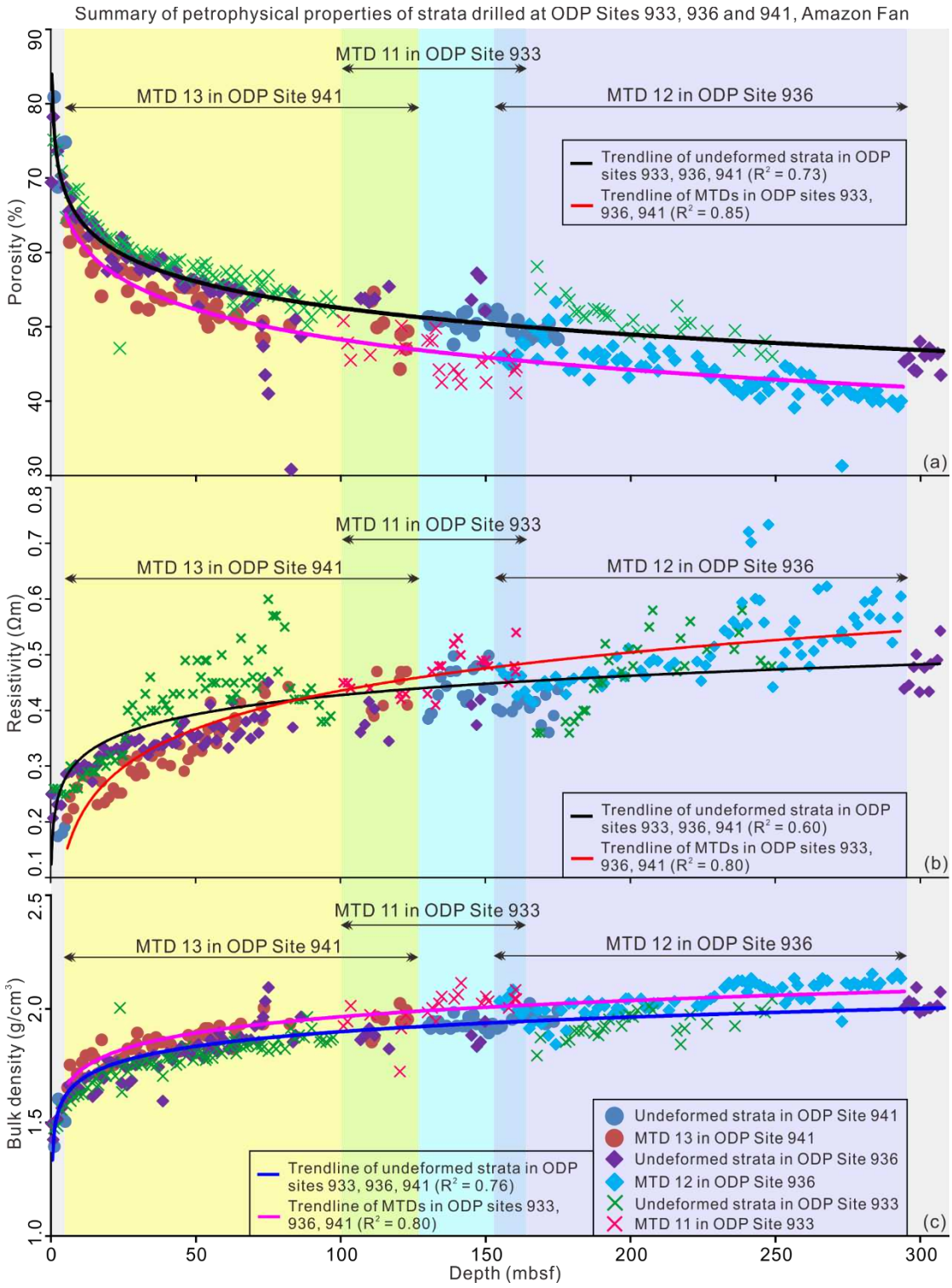

Figure 6: Petrophysical data for ODP Sites 933, 936 and 941 (Expedition 155), Amazon Fan, showing borehole porosity, resistivity, and bulk density.

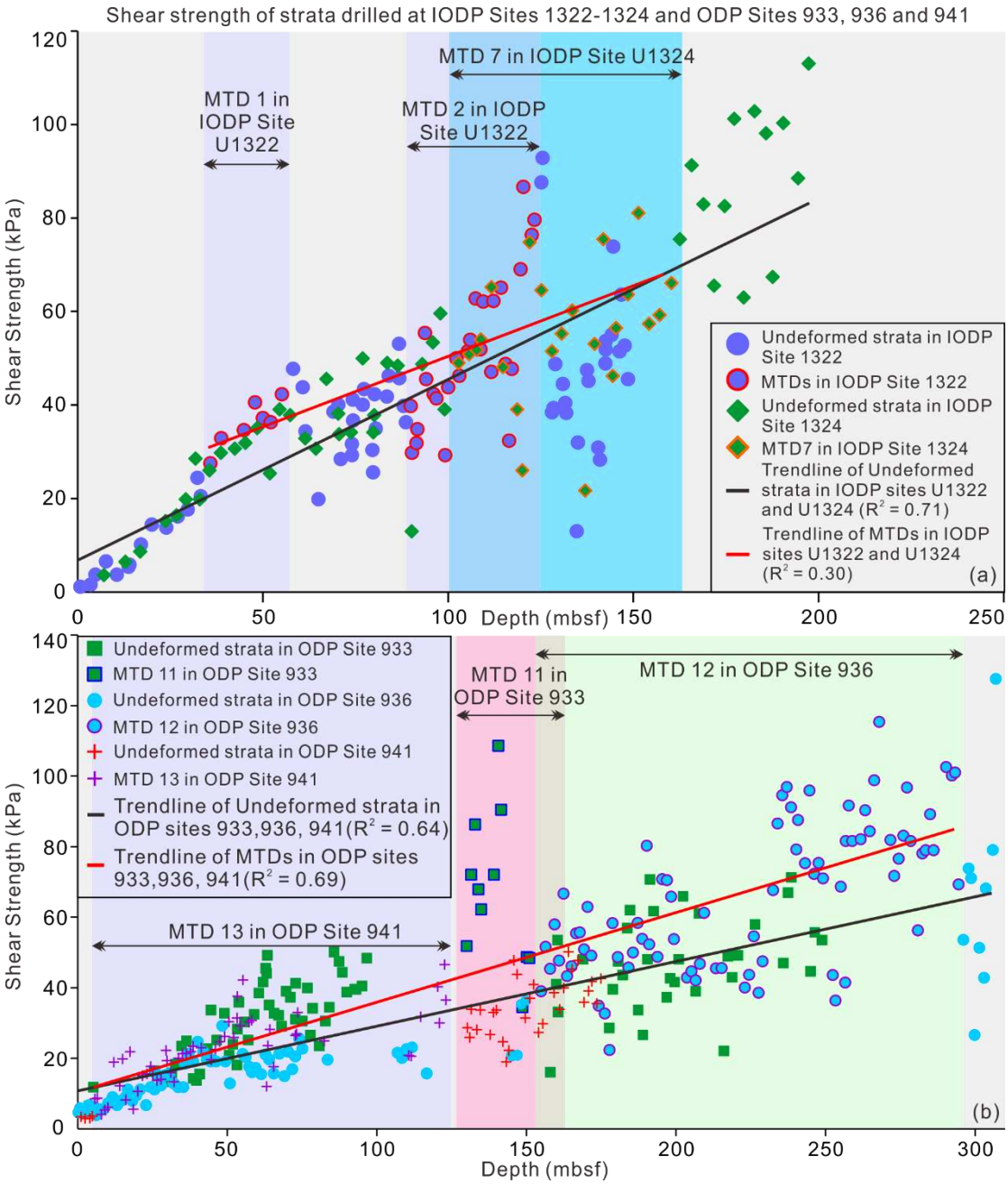

Figure 7: (a) Shear strength of strata at IODP Site U1322 and U1324 in the Gulf of Mexico; (b) Shear strength of strata drilled at ODP Sites 933, 936 and 941, Amazon Fan. The shear strength of MTD intervals (MTD 1-2, MTD 7, MTD 11-13) is generally higher than in undeformed slope strata. It also increases gradually from the top to the base of MTDs.

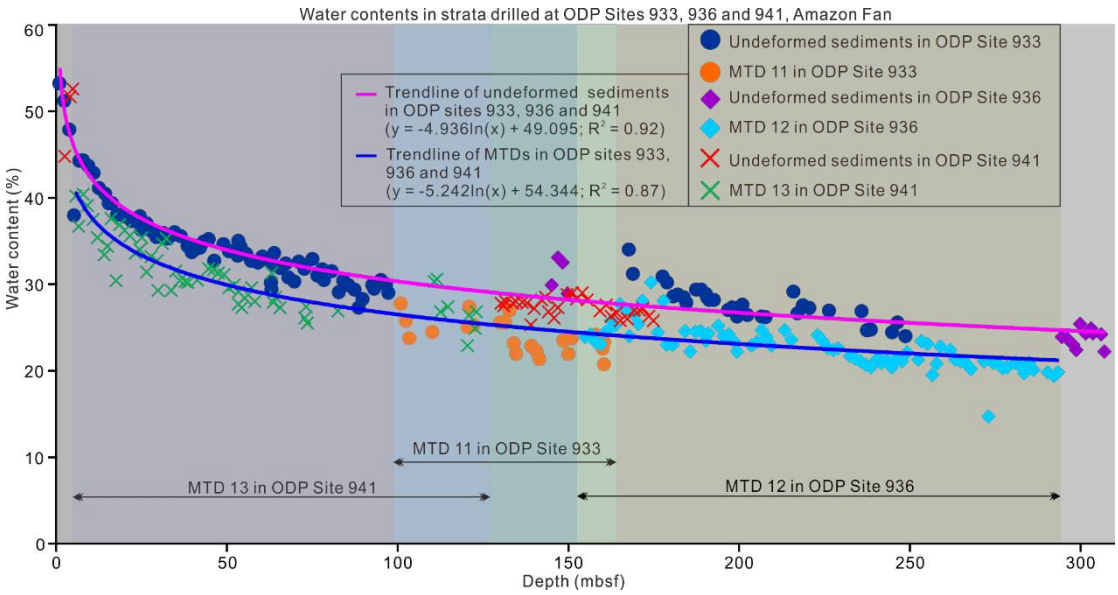

Figure 8: Water content in strata at ODP Sites 933, 936 and 941, Amazon Fan. The water content of MTDs is often lower than in background strata.

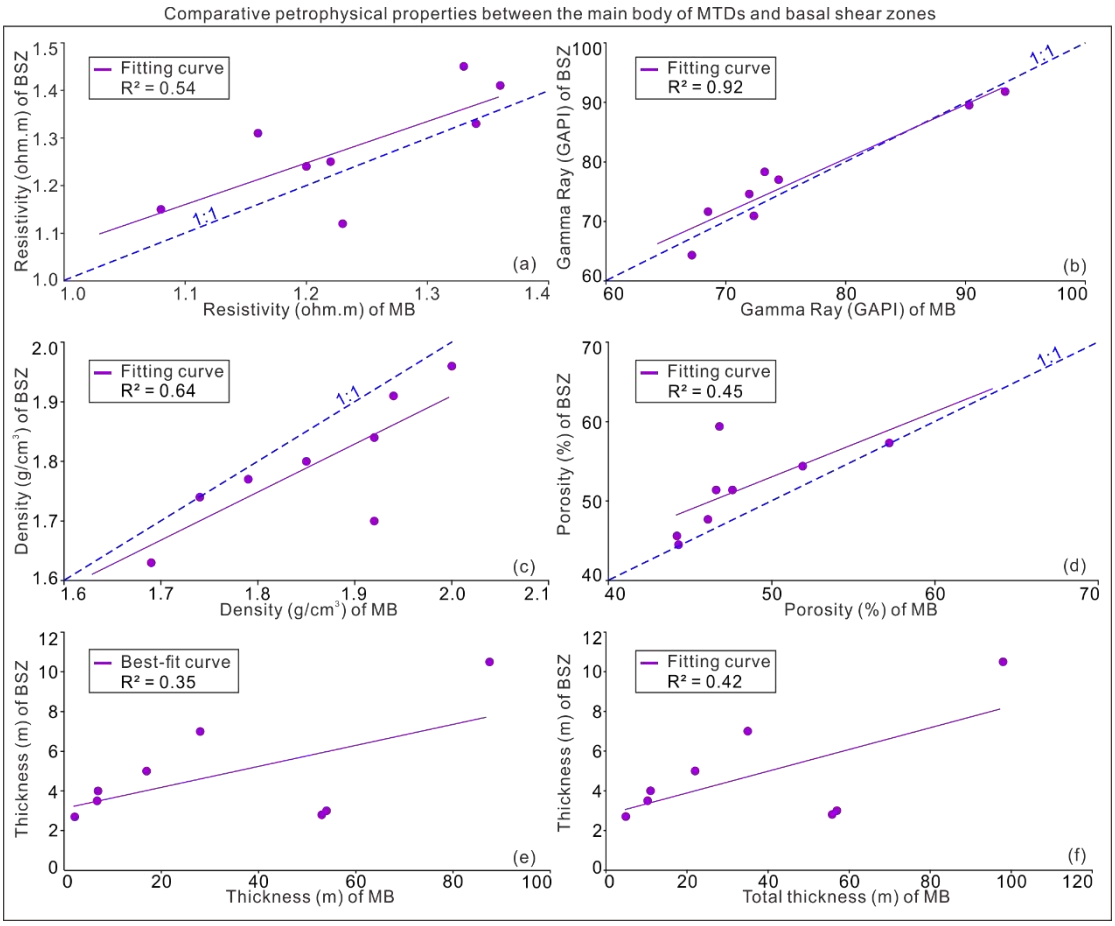

Figure 9: Characteristics of the main body (MB) and basal shear zones (BSZ) of MTDs. (a) Resistivity of BSZ vs. resistivity of MB; (b) Gamma-ray curve of BSZ vs. gamma ray of MB; (c) bulk density of BSZ vs. bulk density of MB; (d) porosity of BSZ vs. porosity of MB; (e) thickness of BSZ vs. thickness of MB; (f) thickness of BSZ vs. total thickness of MTD.

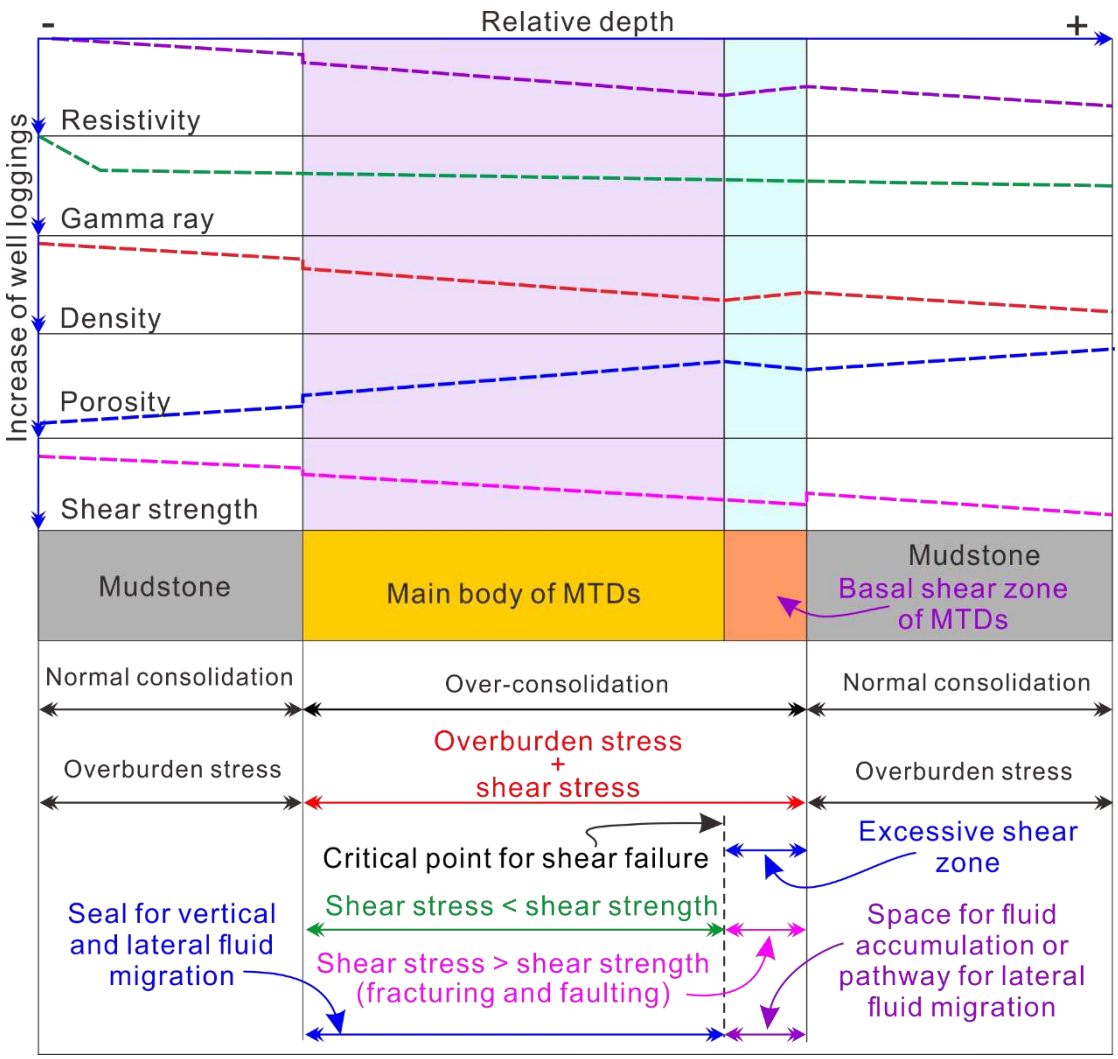

Figure 10: Summaries and interpretations of well-log data for undeformed strata, main body of MTDs, and their basal shear zone(s).

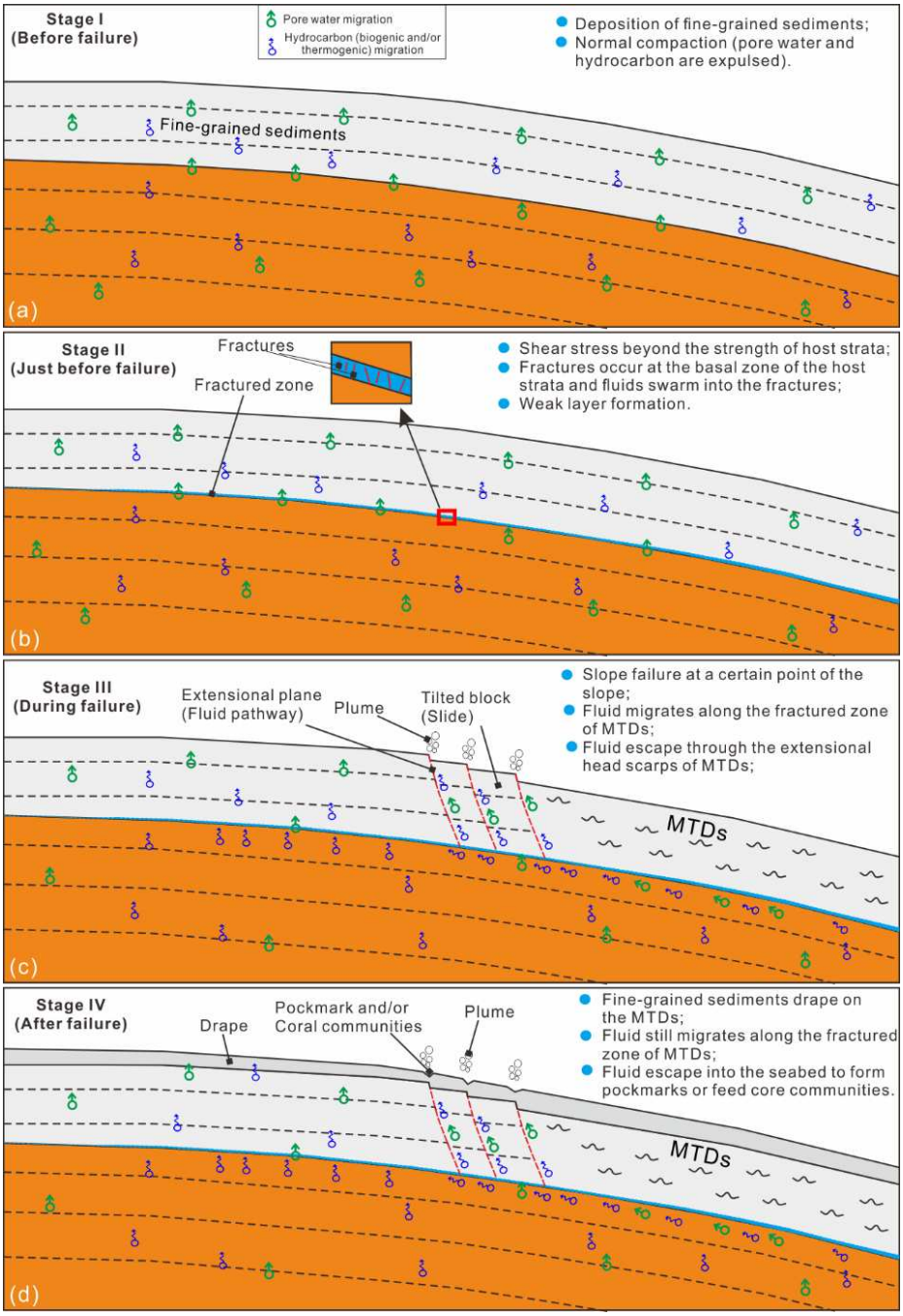

Figure 11: Schematic diagram showing the formation processes of MTDs (under their own gravity) and fluid migration along their basal shear zones. Fractures caused by excessive shear stress at the basal shear zone form a weak layer. These fractures and subsequent fluid charges likely promote the occurrence of slope failure. Fluids escapes onto the sea floor through extensional faults at the upper (head) zones of MTDs during and after their emplacement.

	MTD1					MTD2				
	Overlying strata	MTD	Underlying strata	Overlying strata (%)	Underlying strata (%)	Overlying strata	MTD	Underlying strata	Overlying strata (%)	Underlying strata (%)
Resistivity	0.88	1.04	0.96	18.0	8.0	1.06	1.31	1.05	23.6	24.8
Gamma Ray	64.5	64.34	63.57	-0.2	1.2	68.66	73.93	60.65	7.4	21.9
Caliper	14.05	13.37	13.32	-4.8	0.4	11.70	10.81	10.61	-7.6	1.9
Density	1.59	1.63	1.60	2.5	1.9	1.77	1.89	1.76	6.8	7.4
Porosity	0.67	0.64	0.66	-4.5	-3.0	0.56	0.48	0.56	-14.3	-14.3

=

Table 1: Comparison among the petrophysical characters of MTD 1 and MTD 2, and undeformed strata in the Gulf of Mexico. The data for undeformed strata around MTD 1 include the average values for sediment 10 m above and below the MTD. The data for undeformed around MTD 2 include the average values for sediment 30 m above and 25 m below the MTD.

MTDs		Resistivity (ohm.m)	Gamma Ray (GAPI)	Density (g/cm^3)	Porosity (%)	Thickness (m)
MTD1 (U1322)	MTD strata	1.08	67.16	1.74	57.2	17.0
	Basal shear zone	1.15	64.34	1.74	57.3	5.0
MTD2 (U1322)	MTD strata	1.16	68.5	1.94	44.2	28.0
	Basal shear zone	1.31	71.65	1.91	45.6	7.0
MTD3 (U1322)	MTD strata	1.35	69.48	1.94	45.3	8.0
	Basal shear zone	none	none	none	none	none
MTD4 (U1322)	MTD strata	1.36	72.34	2.00	44.3	7.0
	Basal shear zone	1.41	70.94	1.96	44.5	4.0
MTD5 (U1323)	MTD strata	1.33	73.24	1.92	46.8	87.5
	Basal shear zone	1.45	78.32	1.70	59.4	10.5
MTD6 (U1323)	MTD strata	1.23	71.95	1.92	46.6	54.0
	Basal shear zone	1.12	74.58	1.84	51.4	3.0
MTD7 (U1324)	MTD strata	1.13	86.34	1.85	47.6	49.0
	Basal shear zone	0.95	92.25	1.76	53.2	8.0
MTD8 (UBGH 1-4)	MTD strata	1.20	74.4	1.69	51.9	6.8
	Basal shear zone	1.24	77.0	1.63	54.4	3.5
MTD9 (UBGH 1-4)	MTD strata	1.34	93.3	1.80	46.1	53.0

	Basal shear zone	1.33	91.8	1.85	47.7	2.8
MTD10 (UBGH 1-4)	MTD strata	1.22	90.3	1.79	47.6	2.2
	Basal shear zone	1.25	89.5	1.77	51.4	2.7
MTD11(Site 933)	MTD strata	0.47	none	2.00	45.8	69.7
	Basal shear zone	Unknown	none	Unknown	Unknown	Unknown
MTD12 (Site 936)	MTD strata	0.51	none	2.04	43.9	139.7
	Basal shear zone	Unknown	none	Unknown	Unknown	Unknown
MTD13 (Site 941)	MTD strata	0.33	none	1.85	49.4	124.4
	Basal shear zone	Unknown	none	Unknown	Unknown	Unknown

Table 2: Average resistivity, gamma ray, density, porosity and thickness of the main bodies and basal shear zones of MTDs. Note that the longitudinal resistivity is used at ODP Sites 933, 936 and 941. The term “none” signifies that no basal shear zone developed in a MTDs. The term “unknown” signifies that there is no clear basal shear zone in a MTD because of the sparse sampling or coring.